ANL-83-62

(1)

ANL-83-62

LITHIUM/IRON SULFIDE BATTERIES FOR ELECTRIC-VEHICLE PROPULSION AND OTHER APPLICATIONS

Progress Report for October 1981 – September 1982

ARGONNE NATIONAL LABORATORY, ARGONNE, ILLINOIS

Operated by THE UNIVERSITY OF CHICAGO
for the U. S. DEPARTMENT OF ENERGY
under Contract W-31-109-Eng-38

DISCLAIMER

Printed in the United States of America
Available from
National Technical Information Service
U. S. Department of Commerce
5285 Port Royal Road
Springfield, VA 22161

NTIS price codes
Printed copy: A05
Microfiche copy: A01

Distribution Category:
Energy Storage—Electrochemical--
Advanced Batteries (UC-94cb)

ANL--83-62

ANL-83-62

DE84 004193

ARGONNE NATIONAL LABORATORY
9700 South Cass Avenue
Argonne, Illinois 60439

LITHIUM/IRON SULFIDE BATTERIES FOR ELECTRIC-VEHICLE PROPULSION AND OTHER APPLICATIONS

Progress Report for
October 1981—September 1982

D. L. Barney — Director, Advanced Battery Projects
R. K. Steunenberg — Manager, Lithium/Iron Sulfide Battery Technology
A. A. Chilenskas — Manager, Advanced Battery Technology Development
E. C. Gay — Group Leader, Cell Technology
J. E. Battles — Group Leader, Materials and Post-Test Analysis

September 1983

Previous reports in this series

ANL-79-94	October 1978—September 1979
ANL-80-49	October 1979—March 1980
ANL-80-128	October 1979—September 1980
ANL-81-65	October 1980—September 1981

TABLE OF CONTENTS

TABLE OF CONTENTS (Contd)

LIST OF FIGURES

LIST OF FIGURES (contd)

LIST OF TABLES

LIST OF TABLES (contd)

LITHIUM/IRON SULFIDE BATTERIES FOR ELECTRIC-VEHICLE PROPULSION AND OTHER APPLICATIONS

Progress Report for
October 1981-September 1982

ABSTRACT

This report describes the work done on development of lithium/iron sulfide batteries at Argonne National Laboratory during FY 1982. The work at ANL has been concerned principally with the electrochemical and materials aspects of lithium-alloy negative electrodes and iron sulfide positive electrodes, materials research, cell design studies, and the testing and post-test examinations of cells fabricated by two industrial contractors--Eagle-Picher Industries, Inc. and Gould Inc. Particular emphasis was placed on investigations of alternatives to the present Li-Al and FeS electrodes that would be expected to lead to higher specific energy and power, i.e., investigations concerned with Li-Si, Li-Al-Si, Li-Al-Fe, FeS_2.

Development work by the two contractors consisted of cell design improvements to increase lifetime and specific power and the fabrication of cells for testing in contractor laboratories and at ANL. Eagle-Picher has continued to use two layers of BN felt as electrode separators in its cells, whereas Gould has concentrated its efforts on MgO powder separators, which are believed to offer a near-term cost advantage but are in a somewhat less advanced stage of development.

SUMMARY

Molten Salt Cell Research

Electrochemical Characteristics of Li-Alloy and MS_2 Electrodes

Electrode characterization studies continued in the identification of electrodes suitable for advanced high-performance battery cells. The approach is to evaluate the electrochemical characteristics of the electrodes and the effects that various design and operating parameters have on performance, as well as to investigate voltage losses and voltage-loss processes in the electrodes. The advanced electrode materials studied in this work were Li-Si alloys and FeS_2. The performance characteristics of Li-Al and FeS cell electrodes were also evaluated, and were used as baselines for judging the advanced electrode materials.

Galvanostatic cycling, dc pulsing, and current interruption followed by potential relaxation were the principal techniques used to characterize electrode performance. The experimental cell designs used included a small,

one-dimensional-electrode cell (0.7 cm^2), an open compact bicell, and a sealed compact monocell. In each of these cells, the electrodes contained current collectors that were essentially resistance-free. Hence, electrode-voltage losses were confined to the electrode beds and the electrode current distribution was nearly one-dimensional, i.e., it varied essentially only in the thickness dimension of the electrode. The results of this work have demonstrated the feasibility of each of these cell designs as investigative tools with which to characterize electrode performance. The power characteristics of the electrodes studied varied from very good to fair, depending on the voltage plateau of the electrode material used. Baseline performance values were obtained from the Li-Al and FeS electrodes, the power characteristics of which were found to be very good.

Positive Electrode Research

Several FeS_2 electrode designs were evaluated before one was developed that allowed accurate and reproducible emf measurements for the $FeS_2 \rightarrow Li_3Fe_2S_4$ phase transition. The selected electrode design used a cylindrical, semi-sealed, BN housing equipped with a molybdenum voltage lead. The emf vs. temperature measurements for the above transition were found to be independent of state of discharge in the 4.9 to 31.5% region. Analysis of the data resulted in the following equation, $E(V) = 1.558 + 0.0004785\ T\ (°C)$. The experimental results indicate that reproducible data for this transition can be obtained with increasing or decreasing temperature scans.

An in situ analytical method for the determination of the solubility of iron sulfides in LiCl-KCl electrolyte has been developed. It is based upon converting the dissolved iron sulfide species to Li_2S and upon the Nerstian emf response of the $LiAl/Ni_3S_2$ couple to changes in S^{2-} activity (or concentration at low levels). The method has been used to determine the solubilities of Li_2S and Li_2FeS_2 at 400 and 450°C, respectively, and of FeS_2 at 450°C.

The solubility of Li_2S in LiF-LiCl-LiBr electrolyte was determined to be 6840 ppm at 466°C and 8700 ppm at 498°C. The experiment involved the measurement of the emf of the $Li-Al/Ni_3S_2$ couple at changing Li_2S concentrations; when the Li_2S concentration reaches the saturation value, the emf of the couple becomes constant. After the solubility measurements were completed, emf vs. temperature data for the $Li-Al/Ni_3S_2$ couple were obtained for electrolyte saturated with Li_2S. Comparison of emf data for the $LiAl/Ni_3S_2$ couple in a variety of different electrolytes saturated with Li_2S indicates that the emf of that couple is independent of electrolytic composition.

Hot-Cell Microscopy Studies of Li-Al and Li-Si Electrodes

A technique was developed and used for visual observation of the surfaces of functioning electrodes in molten salts at high temperature. The apparatus used included a stereo-zoom microscope and a hot-stage cell apparatus that contained working and reference electrodes. Experiments were performed with various configurations of Li-Al and Li-Si electrodes to explore the capabilities of this equipment. The resulting observations yielded some tentative conclusions about gas evolution, agglomeration, fines production, and the spatial distribution of the electrode reaction in regard to these electrode systems.

Electrochemical Engineering and Cell Design Studies

Tests of 25- to 35-Ah capacity Li-Al/FeS cells were done to evaluate the lightweight cell design proposed for the experimental cells in the computer cell design studies. The variables investigated included thickness of positive and negative electrodes, theoretical loading density (Ah/cm^3) of the negative electrode, and lithium concentration in the negative electrode. A 0.3 cm-thick positive electrode with a loading density of 1.4 Ah/cm^3 and a Li-Al electrode with a loading density of 0.8 Ah/cm^3 produced the highest utilization at a 3-h discharge rate and highest peak power density at 50% state of charge.

Small-scale Li-alloy/FeS_2 bicells (100 cm^2 electrode area, 30 Ah capacity) are being tested to determine cell performance as a function of active material composition, negative-to-positive capacity ratio, electrode loading density, electrolyte composition, and electrode thickness. Eight Li-Al/FeS_2 bicells have been tested. Similar cells with Li-Si electrodes are also being tested.

The initial version of a computer cell-design program to predict scaled-up cell hardware requirements for given level of performance has been completed. This version permits a verification of the equations in the program and allows an evaluation of its performance forecasting capability.

Equations have been developed to calculate the area specific resistance of Li-Al and FeS electrodes as a function of electrode utilization. Calculated values of area specific resistance agree well with the measured values except at the end of discharge. These equations will be used in the computer cell-design program for Li-Al/FeS cells. Attempts are being made to develop similar equations for FeS_2 electrodes.

Materials Research

Studies have been conducted to characterize the Li-Al alloy reaction with the current-collector and retainer materials of the negative electrodes. These studies showed that the reaction rate is initially controlled by the galvanic deposition of aluminum (from the lithium-depleted Li-Al alloy) onto the current-collector material, which later shifts to a diffusion-controlled reaction. The deposition and diffusion rates were determined.

Protective coatings were investigated as a means of preventing the reaction between aluminum and the current-collector material. The most successful coating material was TiC, which showed no evidence of reaction with aluminum or the current-collector material.

Lithium/FeS Battery Development Program

Testing of Gould and Eagle-Picher Cells

Lifetime testing was done during the year on one group of status cells from Eagle-Picher Industries, Inc. and Gould Inc. The Group IX cells from Eagle-Picher showed an improvement in cycle life over the previous group, Group VI, with a mean time-to-failure of 345, as opposed to 138 cycles. This performance improvement was achieved by suppressing protrusion growth in the negative electrode through reduction of the hole size in the negative-electrode retainers. In present development cells, the hole size is being reduced further, in an attempt to eliminate the protrusion growth entirely.

The cycle life of the Gould cells was also improved. The second group of status cells gave a mean time-to-failure of 330 cycles, compared with 26 and 218 cycles for the previous cell groups. The average specific energies (4-h rate) for the Eagle-Picher and Gould status cells were 90 and 80 Wh/kg, respectively, and the peak power values at 50% state of charge were 80 and 70 W/kg, respectively. Development cells from both contractors showed improvement in power. A Gould development cell gave 130 W/kg and an Eagle-Picher cell gave 104 W/kg. These results were achieved by using larger feedthroughs to lower the ohmic cell resistance.

The characteristics of cells that are continued on cycle after short circuits have developed are being studied. Individual cell tests are carried out to simulate continued operation of a series-connected battery after cell failures have occurred within the battery. Initially, the cell voltage goes negative only near the end of discharge, and the heat generation for discharge and charge is that of a normal, non-shorted cell. With continued cycling (40-190 total cycles as a short-circuited cell), the negative voltage persists for longer periods during discharge and heat generation peaks at 100 W on discharge (three times normal), and at 40-50 W on charge (normally zero). With continued cycling (up to 270 total cycles in the short-circuited condition), the cell reaches an end state with heat generation of 40 W on discharge and 20 W on charge.

ANL Cell Research and Development Program

For state-of-the-art cells resistance mapping measurements were made to determine the resistances of the various current-carrying elements of the cell, to determine component design improvements that will lower cell resistance, and to fabricate and test higher-power cells with the lower-resistance components.

Thermal (freeze-thaw) cycling studies were completed on four engineering-scale Li-Al/FeS bicells with BN felt separators that were either untreated or treated with $LiAlCl_4$ or a magnesium acetate solution as a separator-wetting agent. All cells except the one containing the untreated felt exhibited good capacity stability.

The program goals for the lithium-alloy/FeS electric-vehicle cells are to develop cells of 150 to 350-Ah capacity, specific energy of 125 Wh/kg at the 3-h discharge rate, peak power of 185 W/kg at 50% state of charge, and a 500-cycle mean time-to-failure. Development of such high performance cells requires that particular attention be given to energy-power trade-off studies and to cell designs that improve cycle life. A summary of these trade-off studies is presented. It was concluded that none of the basic state-of-the-art cell designs is sufficient to meet both the specific-energy and the specific-power goals. Improvements are needed in the electrode compositions, to provide higher specific capacity (Ah/g) and/or higher average discharge voltage and better power characteristics.

Post-Test Analysis of Gould and Eagle-Picher Cells

Post-test examinations have been completed of the Eagle-Picher Group I, III, VI, and IX status cells and the Gould Group I and II status cells. In the Eagle-Picher cells, two major failure modes were identified: (1) formation of

Li-Al protrusions that penetrated the BN felt separator and contacted the opposing electrode and (2) extrusion of positive electrode material at the electrode edges as a result of ruptured retainers. The latter failure mode was eliminated by adding an additional retainer around the edges of the electrodes. Studies indicate that Li-Al protrusions can be prevented by adding a fine mesh screen to the normal photoetched retainer on the electrode faces.

The major cause of failure in the Gould cells was penetration of the MgO powder separator by material from the positive electrode. This condition limited the cycle life to 300-500 cycles.

Metallographic examinations revealed that the Li-Al alloy forms a connected, porous structure that remains relatively stable throughout cell life (>1000 cycles).

I. INTRODUCTION

Argonne National Laboratory (ANL) and its subcontractors are developing high-performance lithium-alloy/iron sulfide batteries for electric-vehicle propulsion and for electric-utility system energy storage or storage of energy produced by solar, wind, or other variable sources. The major emphasis, however, has continued to be on the electric-vehicle application. The widespread use of electric vehicles would offer the dual benefits of petroleum conservation and air pollution reduction in congested areas.

During the fiscal period of this report, the research activities of the program were performed at ANL under direction of Lawrence Berkeley Laboratory (LBL) as lead laboratory. Sandia National Laboratories (SNL) provided the lead function for the cell development and testing activities, which were conducted by ANL and two subcontractors--Eagle-Picher Industries, Inc., and Gould Inc.

The cells that are now under development consist of lithium-alloy negative electrodes, FeS or FeS_2 positive electrodes, boron nitride (BN) felt or MgO powder separators, and a molten-salt electrolyte. The LiCl-KCl eutectic electrolyte used in earlier cells has been replaced by other compositions, such as "LiCl-rich" LiCl-KCl (typically, 67 mol % LiCl), LiF-LiCl-KCl, or LiF-LiCl-LiBr. To ensure that the electrolyte remains in a fully molten condition, the cells are customarily operated at a minimum temperature of approximately 430°C.

The details of the electrochemical reactions and the cell designs have been given in preceding reports of this series. The present Li-Al/FeS cells are in a relatively advanced stage of development, and their overall performance capabilities are summarized as follows: specific energy, ∿100 Wh/kg at the 3-h discharge rate; peak specific power, ∿130 Wh/kg at 50% state of charge; cycle life, 300-500 deep discharges. In designing a cell for a specific application, some trade-offs are possible between the specific energy and specific power.

II. MOLTEN SALT CELL RESEARCH

The objective of this program is to meet the performance and lifetime goals for advanced lithium-alloy/iron sulfide electric-vehicle battery cells. These goals are considerably higher than are achievable with the present Li-alloy/FeS cells. The general approach to be used in this research is to utilize more energetic materials in the positive and negative electrodes, thus obtaining higher cell voltages and capacities. The corrosion rates of these more energetic materials will be evaluated through post-test examinations of experimental cells. A computer program is being developed to project the performance of full-scale electric-vehicle battery cells, based on polarization data and other information from small-scale experimental cells.

A. Electrochemical Characteristics of Li-Alloy and MS_2 Electrodes

(L. Redey and D. R. Vissers)

1. Electrode Characterization Techniques

The electrode performance was characterized in these studies by using the dc-pulse and/or the dc current-interruption, potential-relaxation (CIPR) technique. In the dc-pulse technique, the voltage-loss characteristic of the electrodes was investigated by applying a discharge pulse current to the electrode and observing, by use of a reference electrode, the resulting potential drop in the respective working electrodes. The pulse duration was usually 15-30 s. With the CIPR technique, the discharge current was interrupted and the potentials of the electrodes were permitted to relax from their under-load values. Using the reference electrodes, the relaxation of the electrode potentials and the cell voltage were measured, principally in a 1-ms to 15-s time frame, after current interruption. The fast component of the relaxation ($\bar{\eta}_{1ms}$) is believed to be characteristic of the ohmic component of the overpotential, whereas the 15-s relaxation value ($\bar{\eta}_{15s}$) includes a slow relaxation component ($\bar{\eta}_{\Delta t}$) where

$$\bar{\eta}_{\Delta t} = \bar{\eta}_{15s} - \bar{\eta}_{1ms} \qquad (1)$$

The $\bar{\eta}_{\Delta t}$ value relates to the processes that relax and reveal transients in the cell in the time window being observed, such as the electron- and mass-transfer processes, which are influenced by the transmission-line effects. Although the 15-s value represents only ~70-90% of the entire, long-term (10-12 h) voltage relaxation, it can be used conveniently in obtaining experimental data under conditions that are theoretically relevant for electrode characterization.[1]

Normalizing the partial relaxation values ($\bar{\eta}_t$) for current density gives the area-specific resistances, ASR_t (Ω-cm^2). These values are almost independent of the current density in the lower current-density range (0-200 mA/cm^2) and, therefore, can be used in comparing the behavior of different electrodes and cells.

2. Electrochemical Characterization of Baseline Electrode Materials

The advanced state of development and the extensive specific-energy and power characterization of the Li-Al/FeS cell make the electrodes of these cells and their performance characteristics ideal baselines for judging the performance characteristics of other positive and negative electrode materials. Consequently, work to develop such baseline information on the Li-Al and FeS electrodes was carried out during the past year.

A specially designed, compact, prismatic bicell equipped with reference electrodes was used to investigate the voltage losses that occur within the electrodes of the Li-Al/FeS cell. A detailed description of the cell design was presented earlier.[2] The plate area of the electrodes was 53.44 cm^2 and the current collectors consisted of heavy, 0.18-cm-thick sheets of nickel chosen to minimize the ohmic voltage drop in the plates. Consequently, electrode-voltage losses are confined to the electrode beds and the electrode current distribution is nearly one-dimensional, i.e., it varies essentially only in the thickness dimension of the electrode. An important consequence of the one-dimensional current distribution is that the electrochemical reaction across the face of the electrode is much more uniform; thus, the equalizing currents are greatly reduced.

Pulse-current investigations of the Li-Al/FeS bicell indicate that both the Li-Al and the FeS electrodes are capable of delivering very high current densities, even in the 1-1.5 A/cm^2 range, during 15-30 s current pulses (see Figs. 1 and 2). As in any cell system, the electrode materials reveal the general characteristics of the electrodes, namely, the polarization potential sensitivity at any given current density varies with the utilization. The data shown in these figures indicate that the power characteristics of the Li-Al electrode are somewhat superior to those of the FeS electrode.

Area-specific-resistance (ASR) values for the Li-Al and FeS electrodes were evaluated using the CIPR technique. Electrode thicknesses were 0.16 and 0.26 cm for the FeS electrode and 0.30 and 0.49 cm for the Li-Al electrode. The ASR values were determined under various constant-current conditions as a function of state of discharge and near steady-state conditions (i.e., during a constant-current discharge). The ASR values corresponding to a current density of 43, 60 and 270 mA/cm^2 are shown in Figs. 3 and 4 for the FeS and Li-Al electrodes, respectively.

An important observation in this work is that thicker electrodes seem to possess more favorable high-power discharge characteristics than the thinner electrodes.

3. Li-Si Electrode Characterization

Electrochemical characterization studies of advanced electrode materials are being carried out, using small working electrodes with one-dimensional current distribution. The details of the one-dimensional electrode, which ensure that a uniform current distribution is generated across

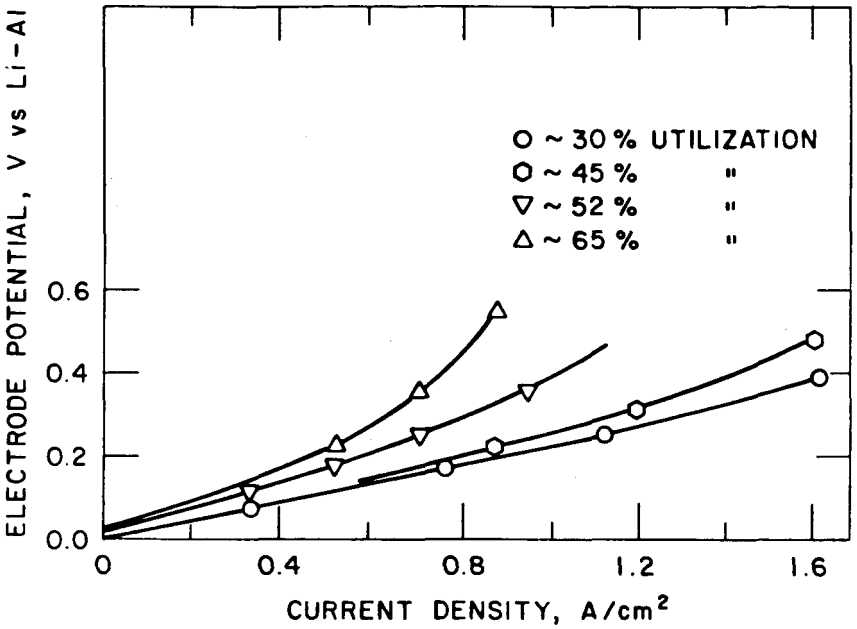

Fig. 1. Voltage-Loss Characteristics of Li-Al Electrode (electrode potential at end of 15-s current pulses; electrode thickness, 0.30 cm; temperature, 460°C)

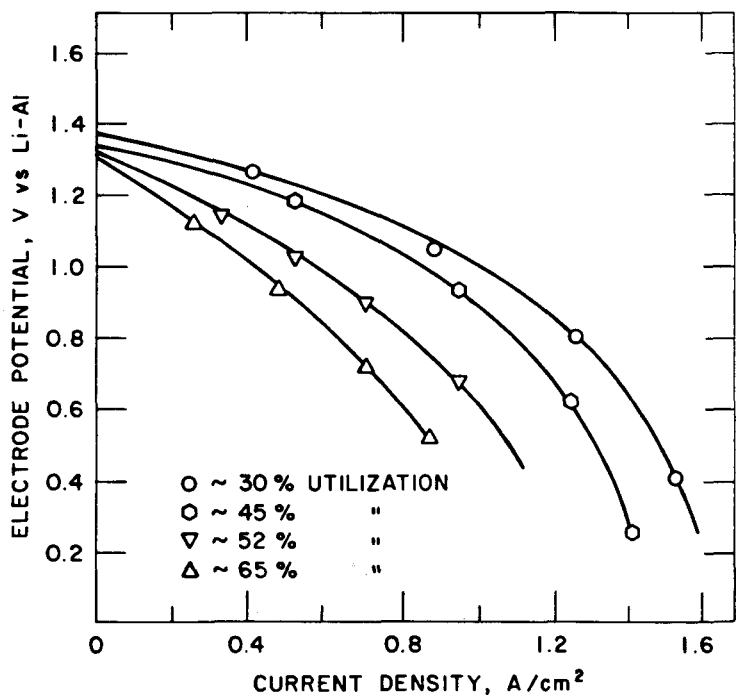

Fig. 2. Voltage-Loss Characteristics of FeS Electrode (electrode potential at end of 15-s current pulses; electrode thickness, 0.16 cm; temperature, 460°C)

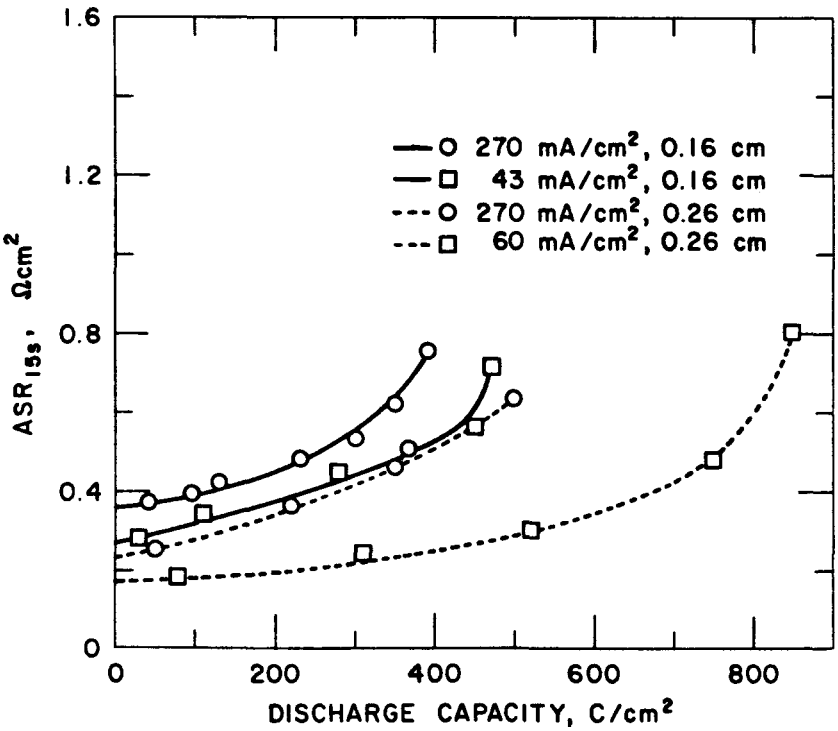

Fig. 3. Area-Specific-Resistance Values of FeS Electrodes (LiCl-rich electrolyte; temperature, 460 °C)

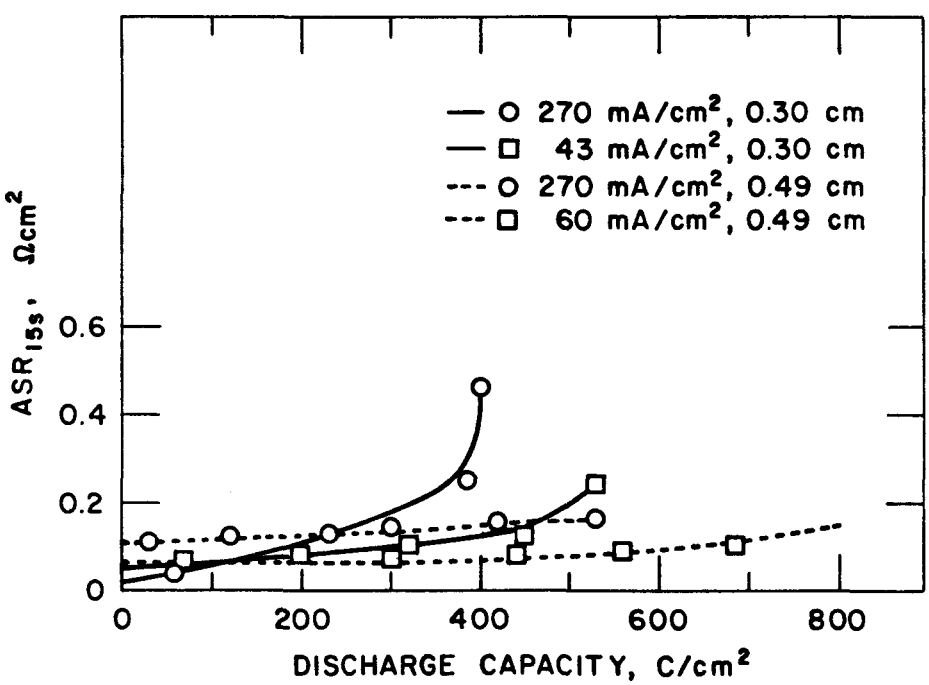

Fig. 4. Area-Specific-Resistance Values of Li-Al Electrodes

the face of the electrode, are given in Fig. 5. The observed power characteristics, polarization, voltage-relaxation values, and calculated ASR of such electrodes can be used to investigate the effects of various parameters on electrode performance, without the hindrance of current-collection problems or the need for compact cell construction.

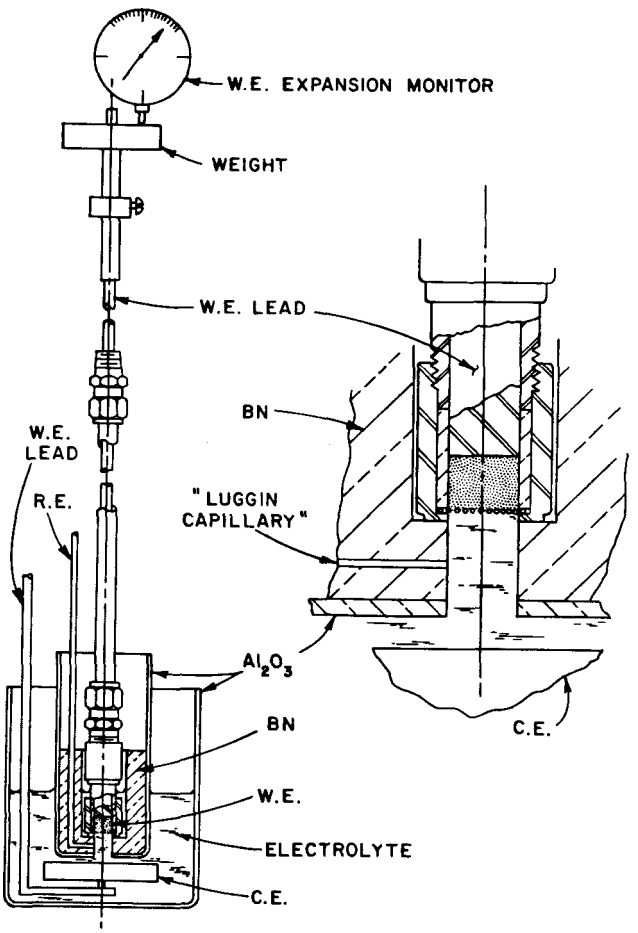

Fig. 5.

One-Dimensional Electrode Configuration (W. E. = working electrode; R. E. = reference electrode; C. E. = counter electrode)

The present one-dimensional electrode design has evolved through several stages. In the initial studies with the one-dimensional electrode, the actual IR-voltage drop that developed in the electrolyte between the reference electrode Luggin capillary and the face of the working electrode was calculated based upon the electrode geometry and specific conductance of the electrolyte, and was therefore somewhat uncertain. In the improved technique now being used, the actual IR-voltage drop in the electrolyte is monitored continuously by two properly located reference electrodes. Another recent improvement in the design provides a nearly constant thickness of the working electrode, which is operated under constant mechanical load (0-500 kPa). The bed thickness is monitored to a resolution of ±10 μm, assuming negligible expansion at the front electrode surface. The electrode bed pressures can be monitored to a resolution of ±10 kPa.

Results from the one-dimensional electrode studies indicate that the Li-Si electrode operates well over a wide range of lithium compositions. Two such electrodes and their performance are described in Table 1. It is interesting that the ASR values decreased with increased electrode thickness. In operating the electrodes, (1) the ASR_{15s} values increased on the respective Li-Si voltage plateaus as lithium was discharged from the electrode, and (2) a sharp drop in the ASR_{15s} values was observed as the discharge reaction shifted from one plateau to the next (see Fig. 6). Anomalous (very high) ASR values observed after extended cycling are believed to have resulted from an electrolyte-level problem caused by breakage of the inner Al_2O_3 crucible (see Fig. 5).

Table 1. Preliminary ASR_{15s} Values for Li-Si Electrodes at 460°C

	ODE-20	ODE-21
Li-Si Electrode		
Thickness, cm	0.6	0.4
Capacity		
kC	1.81	1.15
kC/cm^3	4.24	4.04
Approximate Electrode Compositions	ASR_{15s} Values, Ω-cm^2	
$Li_{3.17}Si$	0.277[a] (0.374)[b]	0.514[c]
$Li_{2.5}Si$	0.347 (0.450)	0.704
$Li_{2.2}Si$	0.277 (0.380)	0.588
$Li_{1.9}Si$	0.443 (0.530)	0.871
$Li_{1.7}Si$	0.390 (0.550)	0.595
$Li_{0.95}Si$	0.600 (0.730)	1.100

[a]Discharge number 4, 42 mA/cm^2.

[b]Discharge number 8, 100 mA/cm^2.

[c]Discharge number 2, 42 mA/cm^2.

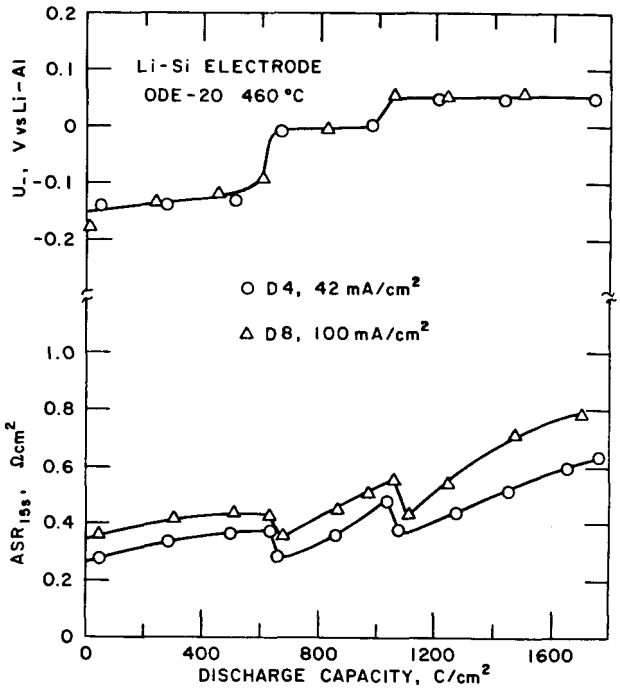

Fig. 6.

Discharge Characteristics of Li-Si Electrode

The power characteristics of the Li-Si electrode were measured on three of the Li-Si voltage plateaus ($Li_{3.25}Si$-$Li_{2.33}Si$, $Li_{2.33}Si$-$Li_{1.71}Si$, and $Li_{1.71}Si$-Si). The results of these pulse-current studies (see Fig. 7)

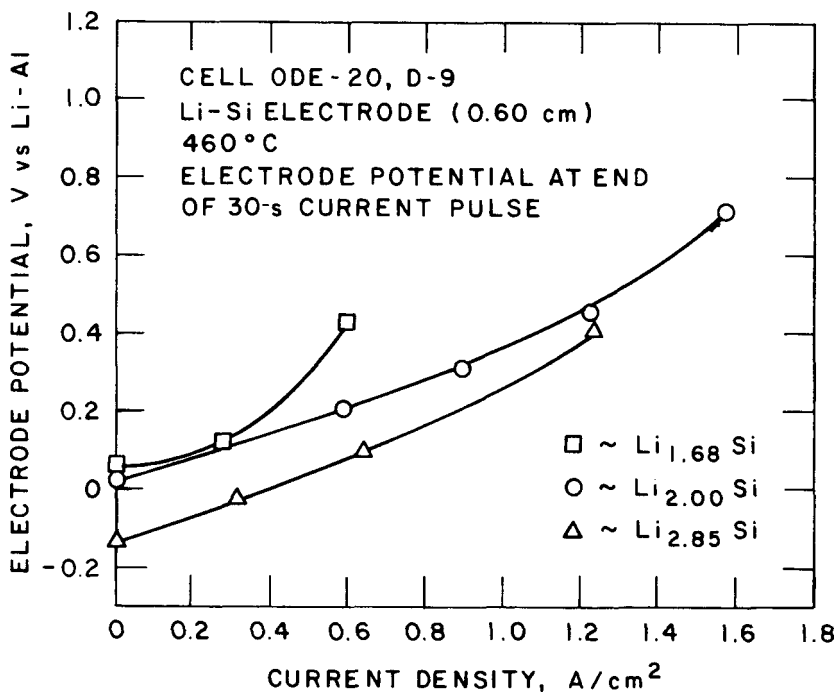

Fig. 7. Power Characteristics of Li-Si Electrode

indicate good power characteristics on all but the $Li_{1.71}Si$-Si plateau. The poor power characteristics probably resulted from the formation of elemental silicon on the surfaces of the $Li_{1.71}Si$ particles. Lithium solubility and diffusion in silicon are both very low.

Post-test examinations of the electrodes indicated the formation of an extensive, uniformly distributed corrosion layer on the nickel Retimet current collector (see Fig. 8), but separate from the nickel base metal. The gradual formation of this layer could be responsible, in part, for the observed increase in the ASR_{15s} values with cycling. Further studies are being carried out to determine the composition of the corrosion-layer material.

4. Li-Si/FeS_2 Sealed Compact Cell Studies

The objective of these studies was to evaluate the performance characteristics of the Li-Si and FeS_2 electrodes in sealed, compact cells. The cell design used in this work was changed from that of an open, compact bicell, which utilized two positive and two negative electrodes in a parallel array,[2] to that of a sealed, compact simple cell, or monocell design with one positive and one negative electrode (see Fig. 9). Although the current collectors used in the respective electrodes of the compact monocell are the same as those used in the bicell, the elimination of the parallel electrode design should tend to maintain the one-dimensional current distribution and ensure a more-uniform current distribution on the faces of the respective electrodes. With the parallel plate design, slight resistance variations in the charge (ion or electron) transfer system could cause significant differences in the current density on the negative or positive plates.

The use of a sealed cell design to avoid sulfur loss at the cell operating temperature does create a problem for the electrode characterization studies. Because these studies require the use of the Ni/Ni_3S_2 reference electrode-thermocouple double sensor, and because a sealed feedthrough for the sensor did not exist, it was necessary to develop a suitable device for the purpose. Such a semi-elastic seal between the metal cell can and the alumina tube of the reference electrode has been developed by using a 1/8-in. ($\sim$3 mm) Swagelok fitting, in which the front ferrule is removed and replaced with several loops of BN yarn.

A description of the first sealed monocell, MC-1, is given in Table 2. The cell was fabricated in the partially charged state, and nickel Retimet was used in the negative electrode, to improve current collection and morphology of the Li-Si electrode.

Characteristic potentials and ASR_{15s} values for the respective electrodes of Cell MC-1 are shown in Figs. 10 and 11 for 37 and 74 mA/cm^2 discharges, in that order. The reproducibility of the measurements is excellent, and the measurements indicate that in the $FeS_2 \rightarrow Li_3Fe_2S_4$ transition region, significant ASR_{15s} values develop in the FeS_2 electrodes. The ASR_{15s} values for the Li-Si electrode are similar to those observed in the one-dimensional electrode studies.

During charge (18.5 mA/cm^2), the ASR_{15s} values (see Fig. 12) are similar to those that were observed earlier for the Li-Al/FeS cell.[3]

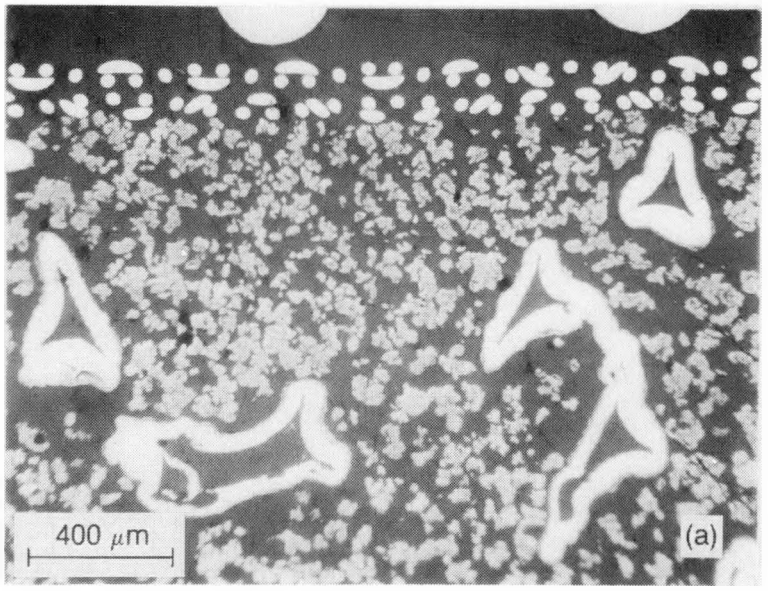

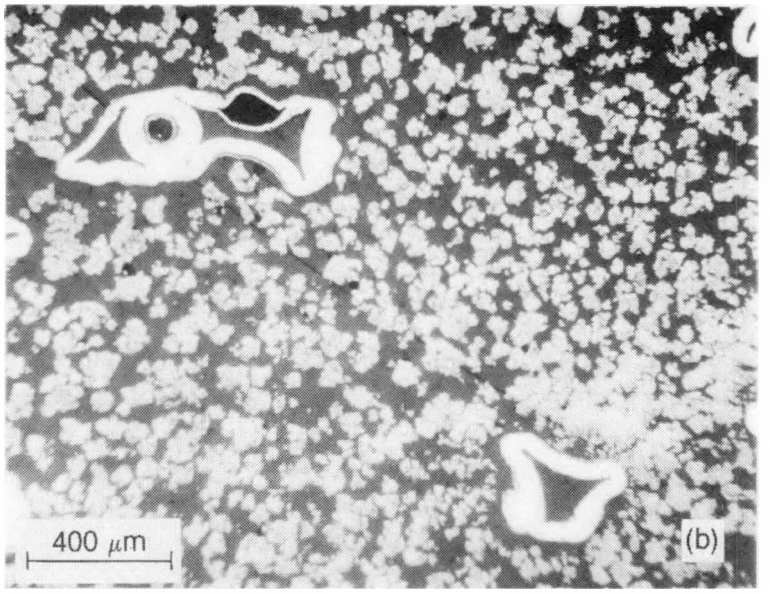

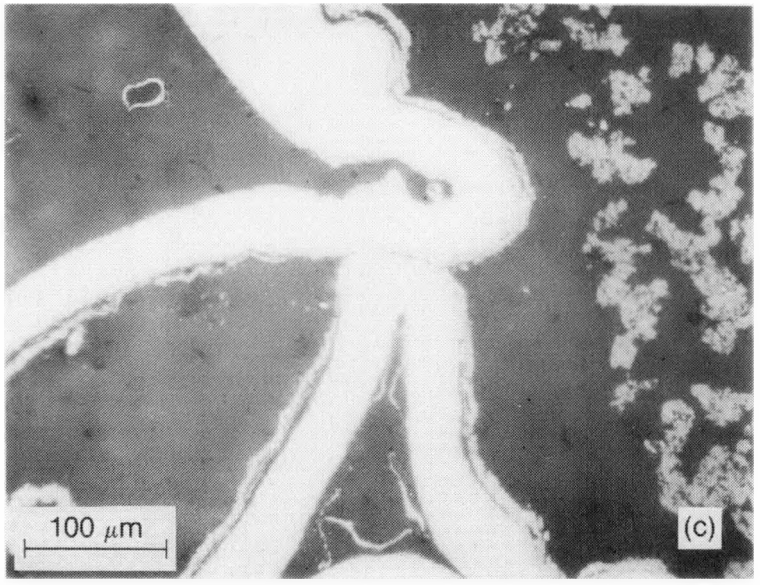

Fig. 8.

Photomicrographs Showing Sections of the Li-Si Electrode: (a,b) morphology of Li-Si electrode and (c) corrosion of nickel Retimet current collector in Li-Si electrode

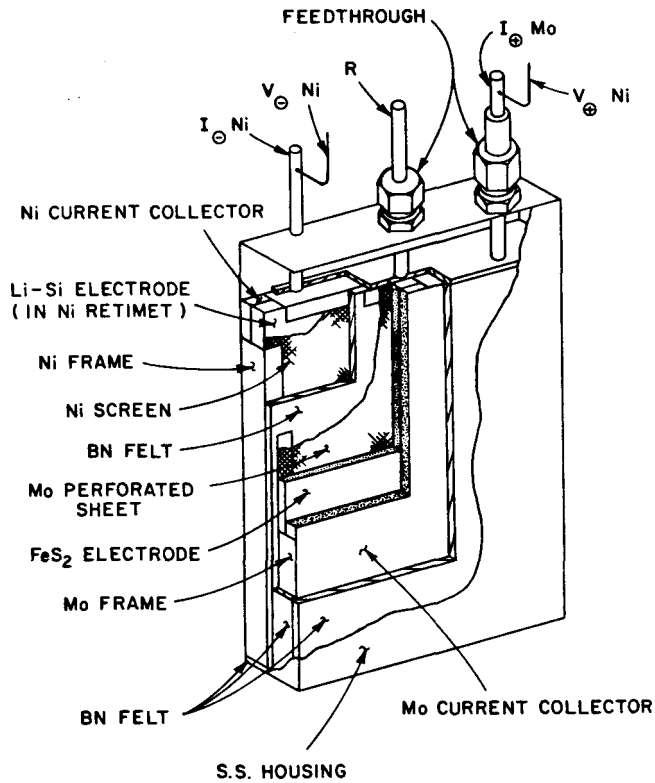

Fig. 9.

Monocell Design

Table 2. Description of Monocell MC-1

	FeS_2 Electrode	Li-Si Electrode
Area, cm^2	53.44	53.44
Thickness, cm	0.3	0.5
Capacity, kC (Ah)	64.8(18)	97.2(27)
Loading Density, kC/cm^3	4.0	3.64
Current Collector Plate Thickness, cm	0.6[a]	0.5[b]
Initial Charge State	Li_2FeS_2	Li_2Si

[a]Plate made of molybdenum.

[b]Plate made of nickel.

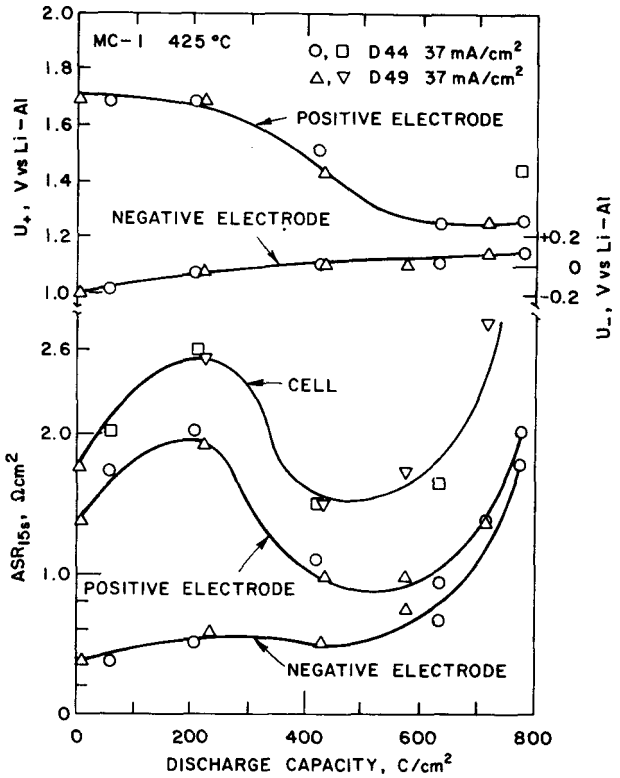

Fig. 10.

Discharge Characteristics of Test Monocell (37 mA/cm^2)

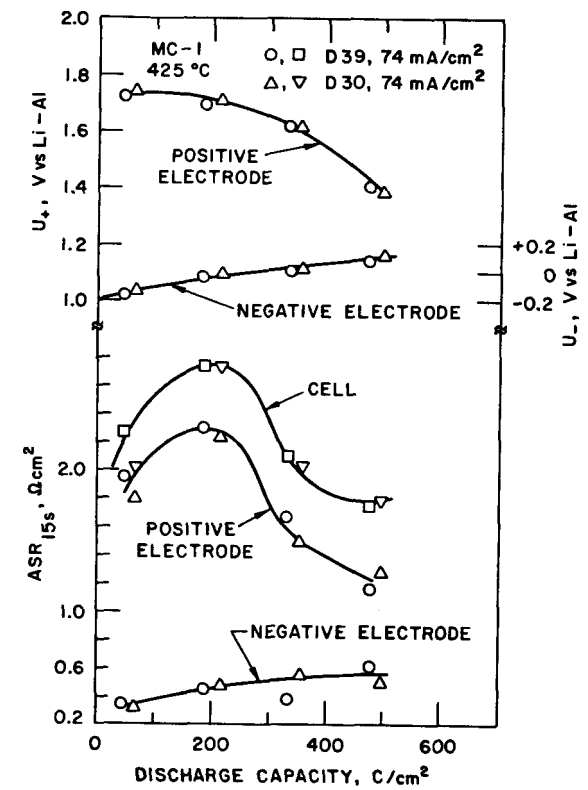

Fig. 11.

Discharge Characteristics of Test Monocell (74 mA/cm^2)

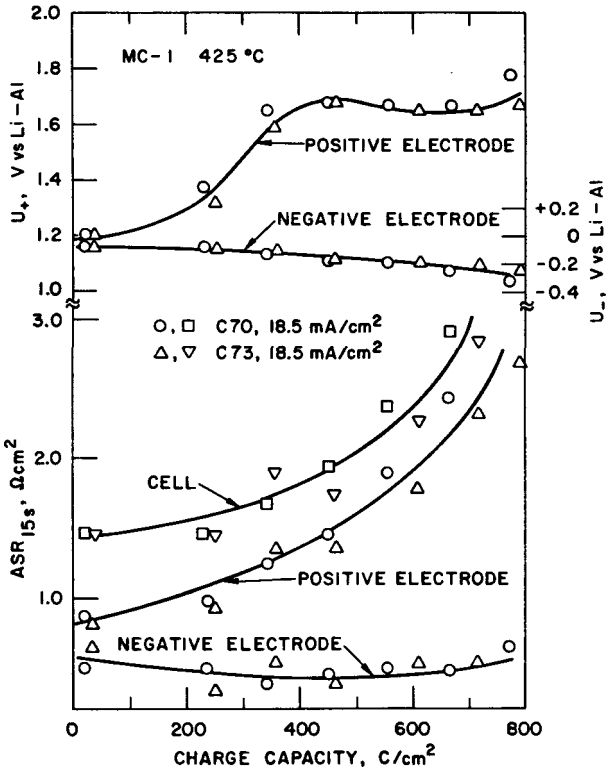

Fig. 12.

Charge Characteristics of Test Monocell (18.5 mA/cm^2)

Although the electrodes in MC-1 have not been optimized for thickness or loading density, their performance characteristics are very reproducible. The ASR_{15s} values of the Li-Si electrode are very similar to those that might be predicted from the one-dimensional electrode studies, suggesting that this technique can be used to evaluate the effects of various parameters on the performance of the respective electrodes. Further optimization of the Li-Si and FeS_2 electrodes is necessary before valid comparisons of their performance can be made with the baseline values of the near-optimized Li-Al and FeS electrodes.

B. Positive Electrode Research

(Z. Tomczuk and D. R. Vissers)

1. Emf Measurement of FeS_2 Electrode Phase Transitions

As Li-Al/FeS_2 cells are discharged, the positive electrode undergoes a series of phase changes, which are in the sequence

$$FeS_2 \rightarrow Li_3Fe_2S_4 \rightarrow Li_{2+x}Fe_{1-x}S_2 \ (x \approx 0.2) + Fe_{1-x}S \rightarrow Li_2FeS_2 \rightarrow Li_2S + Fe$$

During the same time, the LiAl electrode undergoes a single phase change that is the formation of α-Al from β-LiAl. The emf values of the transitions that take place in the FeS_2 electrode *vs.* α-Al + β-LiAl as a function of temperature must be known if a complete thermodynamic description of the Li-Al/FeS_2 system is to be developed. Therefore, the efforts of the past year have been directed toward obtaining this information. However, as the experimental work was begun, it became clear that there were difficulties in obtaining reliable data for the $FeS_2 \rightarrow Li_3Fe_2S_4$ transition. Consequently, much of the past year's effort was directed toward developing a suitable cell design for making the emf measurements.

Various cell designs were used in this effort. The first was identical to that, previously described, for the FeS electrode measurements.[4] However, this design was abandoned after three identical cells failed to yield reproducible emf data. One common characteristic of these cells was that the emf drifted at a given temperature, perhaps as a result of high self-discharge rates. In each case, post-test examination found metallic particles exterior to the positive electrode housing; it seems possible that short-circuit paths were generated between the electrodes by the formation of metallic bridges, causing drifting emf values.

To circumvent the problems associated with the earlier FeS_2 electrode designs, the design was changed to restrict the area of the interface between the electrode bed and the bulk electrolyte of the cell. In this design, the positive electrode housing was constructed from two threaded ATJ graphite cylinders which, when joined, formed the electrode housing and generated a Luggin capillary for the electrode. The partially slotted-thread design permitted continuous variation of the cross-sectional area of the Luggin capillary at cell operating temperature, by simply changing the extent to which the upper cylinder section of the electrode housing was threaded into the lower. The lower graphite cylinder in the design was mounted rigidly to a molybdenum base plate, and a 1/4-in. OD molybdenum rod attached to the upper cylinder served as the voltage lead for the electrode.

Reproducible emf data for the $FeS_2 \rightarrow Li_3Fe_2S_4$ phase transition were obtained with this design. However, data were still not reproducible from cell to cell; for example, at the same temperature, the emf values differed by as much as 40 mV. As with the earlier cells, metallic particulate material was found external to and in contact with the graphite housing, suggesting that a "mixed potential" value was being measured, rather than the emf value for the equilibrium phase transition.

To avoid the mixed potential problem, the FeS_2 electrode housing was constructed from BN, an electronic insulator (see Fig. 13). With this new electrode design, it has been possible to obtain reproducible emf data at different temperatures and from cell to cell.

A total of 21 data points were obtained in these studies, at various states of discharge over the temperature range of 382 to 455°C. The experimental results are shown in Fig. 14 and can be represented by the equation

$$E(V) = 1.5558 + 0.0004785T(°C) \qquad (2)$$

The correlation coefficient for the data represented by this equation is 0.996. The data points used were all from long-term measurements (>100 min at given temperature, with emf fluctuations of less than 0.1 mV over the time period).

The experimental points are numbered consecutively in Fig. 14. They indicate that reproducible data were obtained with measurements made for increasing or decreasing temperature, as well as at increasing state of discharge. The theoretical states of discharge of the electrode for the respective points were: points 1-8, 4.9%; points 9-13, 5.9%, with point 9 being obtained at the same temperature as point 8 (the difference in emf between these points was 0.16 mV); points 14-16, 13.3%; points 17-18, 15.8%; point 19, 16.8%; point 20, 28.9%; and the last point, 21, was obtained at 31.5%. At point 21, the

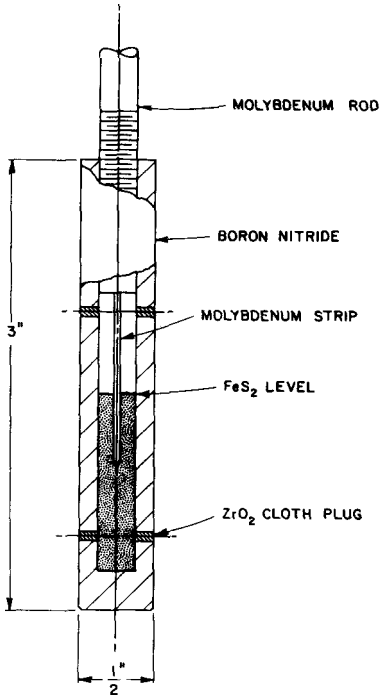

Fig. 13.

FeS_2 Electrode Design for Emf Measurements

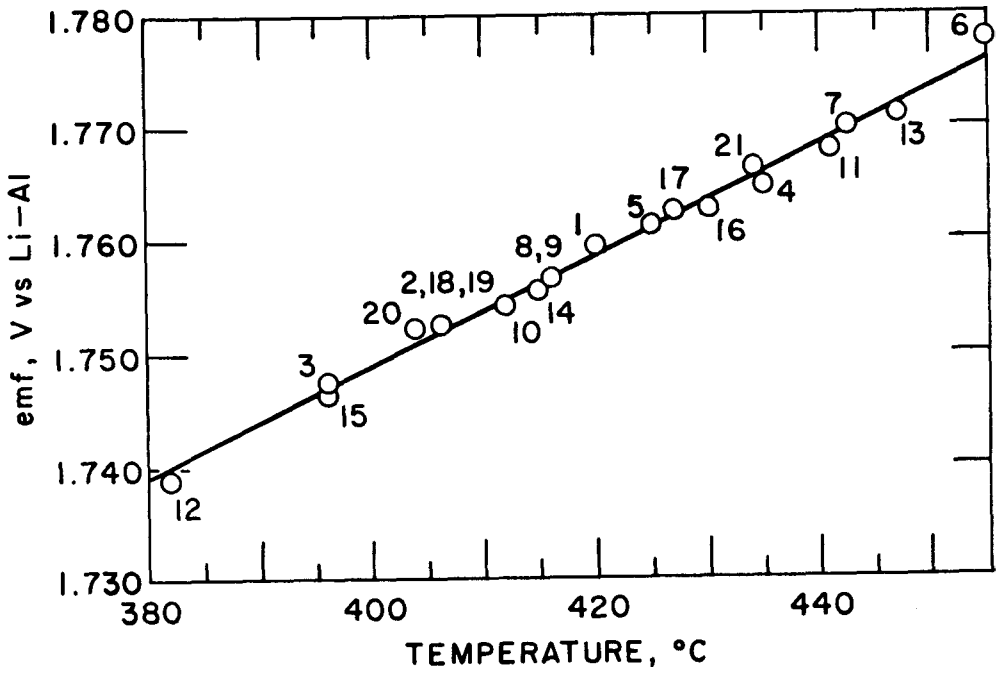

Fig. 14. Emf vs. Temperature Curve for the $FeS_2 \rightarrow Li_3Fe_2S_4$ Transition

cell had been discharged into the $Li_3Fe_2S_4$ + $Li_{2+x}Fe_{1-x}S_2$ ($x \simeq 0.2$) + $Fe_{1-x}S$ region. However, before reliable emf values could be obtained as a function of temperature, the BN housing shattered, resulting in a short circuit. Therefore, the cell test had to be terminated. The BN shattered as a consequence of the forces generated in the housing by the expansion of the electrode materials during the discharge. In this electrode, insufficient volume has been provided for the expansion created by the FeS_2 + $Li_3Fe_2S_4$ transition.

The results of this work indicate that accurate and reproducible emf vs. temperature data can be obtained for the FeS_2 + $Li_3Fe_2S_4$ transition if the proper experimental techniques are used. These measurements indicate that the data are independent of state of discharge within the FeS_2 + $Li_3Fe_2S_4$ region and, therefore, provide additional support for the phase diagram and coulometry data previously reported.[4] The positive temperature coefficient of this transition emf (see Eq. 2) indicates that the entropy change for the transition results in a significant entropic heat absorption process for the discharge of the electrode (0.3340 W/A); this phenomenon will aid greatly in the thermal management of a Li-M/FeS_2 battery during discharge.

2. Solubility of Iron Sulfide in LiCl-KCl Electrolyte

The positive electrodes of Li-Al/FeS and Li-Al/FeS_2 cells both undergo a series of phase changes as they are ultimately discharged to Li_2S and iron. With the exception of Li_2S, the solubilities of these phases as a function of temperature were not known quantitatively. Qualitatively, the solubilities must be low at cell operating temperatures because the cells exhibit low self-discharge rates. However, from both practical and theoretical points of view, it is important to know what these solubility values are in LiCl-KCl eutectic electrolyte. Hence, effort was directed during the past year toward the development of an analytical technique that would allow quantitative determinations of the solubility values of the iron sulfides.

The analytical method developed is an in situ method and is based on the Nernstian response of the emf of the Li-Al/Ni_3S_2 couple to changes in the Li_2S activity (or concentration at low levels). An important advantage of this method is that it eliminates the problems associated with obtaining a representative sample and the handling difficulties, such as keeping the sample in a moisture-free environment. In addition, the method is accurate for low levels ($\sim$25 ppm) of sulfide; most wet chemical methods either will not measure such low levels or are very difficult to execute if accurate results are to be obtained.

The analytical method can be used for most metal sulfides and involves the following steps: (1) equilibration of the liquid LiCl-KCl with the desired solid metal sulfide, (2) removal of the undissolved metal sulfide from the electrolyte, (3) reduction of the metal sulfide in solution by LiAl, to yield Li_2S and the metal, (4) formation of Ni_3S_2 by anodizing a nickel rod, which is placed in the melt after the reduction step is completed, and (5) measuring of the emf for the Li-Al/Ni_3S_2 couple. The Li_2S concentration in solution is then determined, using a working curve generated previously. This method was used to determine the solubilities of Li_2FeS_2 (an intermediate phase in both the FeS and FeS_2 electrodes) and Li_2S, as well as to investigate the solubility of FeS_2 in LiCl-KCl eutectic electrolyte.

The working curve was obtained by measuring the emf of the Li-Al/Ni_3S_2 couple for known Li_2S concentrations, which were generated by adding weighed amounts of Li_2S to the LiCl-KCl electrolyte. The Ni/Ni_3S_2 electrode was formed by anodizing a Ni-200 rod (0.6 cm dia, 10 cm^2 area), using an intermittent anodic current ($\sim$10 $\mu A/cm^2$, $\sim$0.1 C/cm^2). The emf of the Li-Al/Ni_3S_2 couple was measured about four hours after each addition of Li_2S at 400°C, then measured again after the temperature had been increased to 450°C. The stability of the observed emf value was within ±1 mV for >16 h. For the Li_2FeS_2 and FeS_2 solubility measurements, $\sim$1 g of Li_2FeS_2 or FeS_2 powder was placed within a molybdenum cup, where the powders were confined by the use of 100 mesh molybdenum screen and zirconium cloth. The equilibration time at temperature was $\sim$300 h and the reduction time with Li-Al was $\sim$70 h. These times were chosen arbitrarily and probably could be reduced significantly if the solutions were stirred. However, because of possible contamination, it was decided not to use stirring in this study.

The working curve obtained is shown in Fig. 15, and it supports the claim of Redey and Vissers[4] that the Ni/Ni_3S_2 electrode potential obeys the Nerst equation. From the breaks in the curves of Fig. 15, the solubility of Li_2S in LiCl-KCl eutectic was determined to be 780 ppm at 400°C and 980 ppm at 450°C. These values agree well with those obtained by the cyclic voltammetric procedure.[5] Cyclic voltammetry was tried but could not be used for the iron sulfides because of the competing reaction of iron and Li_2S, which takes

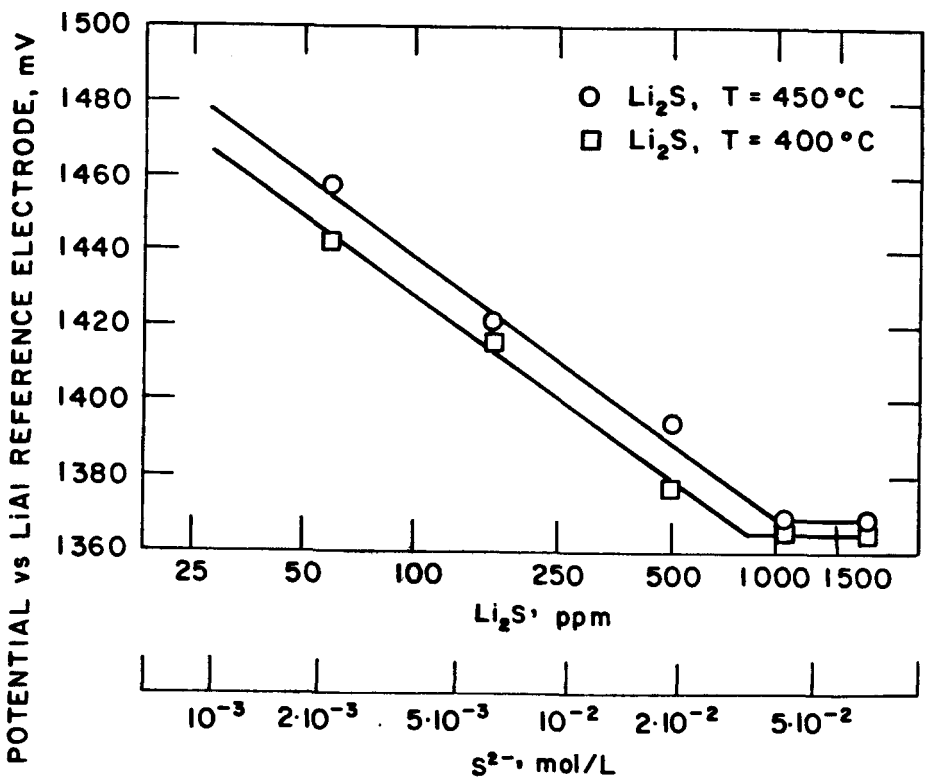

Fig. 15. Emf vs. Li_2S Concentration for the Li-Al/Ni_3S_2 Couple

place in the same potential region where Li_2S is oxidized. The concentrations of Li_2S generated from the dissolved Li_2FeS_2 were 2.06 ± 0.14 x 10^{-2} mol/L at 400 °C and 2.28 ± 0.16 x 10^{-2} mol/L at 450 °C. The Li_2S generated from dissolved FeS_2 at 450 °C was 1.02 ± 0.09 x 10^{-2} mol/L.

The analytical data obtained for Li_2FeS_2 were used to calculate the free-energy change for the reaction,

$$Li_2S + FeS \rightarrow Li_2FeS_2 \qquad (3)$$

Our analytical results yield values of 1.5 ± 1 and 2.6 ± 1.0 kJ at 400° and 450 °C, respectively. Because these calculated free-energy values agree well with those derived earlier using emf data obtained with the FeS electrode,[6] the analytical method appears to be producing satisfactory results.

3. Solubility of Li_2S in LiF-LiCl-LiBr Electrolyte

Work with the LiF-LiCl-LiBr electrolyte in the past year was directed toward completing the Li_2S solubility measurements in the different molten-salt electrolytes and determining the emf-*vs*.-temperature characteristics of the Li-Al/Ni_3S_2 couple in the different electrolytes saturated with Li_2S. These experimental values are important in providing information on how the electrolyte composition affects the electrochemical characteristics of FeS and FeS_2 electrodes. In the previous year,[7] the solubility of Li_2S in the electrolytes was shown to increase in going from KCl-rich LiCl-KCl to LiCl-KCl eutectic, and then to LiCl-rich LiCl-KCl. The corresponding emf *vs*. temperature curves for the LiAl/Ni_3S_2 couple in these electrolytes saturated with Li_2S were also reported.

The general procedure in making the solubility measurements consisted of adding a weighed amount of Li_2S to the LiF-LiCl-LiBr electrolyte, allowing sufficient time for dissolution of the added Li_2S, anodizing a Ni-200 rod to form Ni_3S_2, and measuring the emf of the Li-Al/Ni_3S_2 couple. At the end of each measurement, more Li_2S was added and the procedure was repeated until the electrolyte contained Li_2S in excess of saturation. The Li-Al electrode for these tests contained ∿2.0 g of Li-Al alloy (∿38 at. % Li) and had a nickel current lead to eliminate any possible thermal emf contribution to the measured emf. The time required to reach equilibrium emf value after formation of Ni_3S_2 was typically 20 min, and the emf value was stable at a given temperature for periods >1 h. The amount of Ni_3S_2 formed ranged between 1 and 10 coulombs. The temperatures tested were 466 and 498 °C.

The experimental results for the solubility determination are shown in Fig. 16, in which the break points in the emf *vs*. log Li_2S concentration relationship occur at 6840 ppm at 466 °C and 8700 ppm at 498 °C. These values represent the solubility of Li_2S in this electrolyte at the respective temperatures. The observed potential changes of 76.4 and 70.1 mV per decade change in S^{2-} concentration (or activity) at 498 and 466 °C, respectively, agree well with those predicted for a two-electron change, namely 76.5 and 73.3 mV at the respective temperatures.

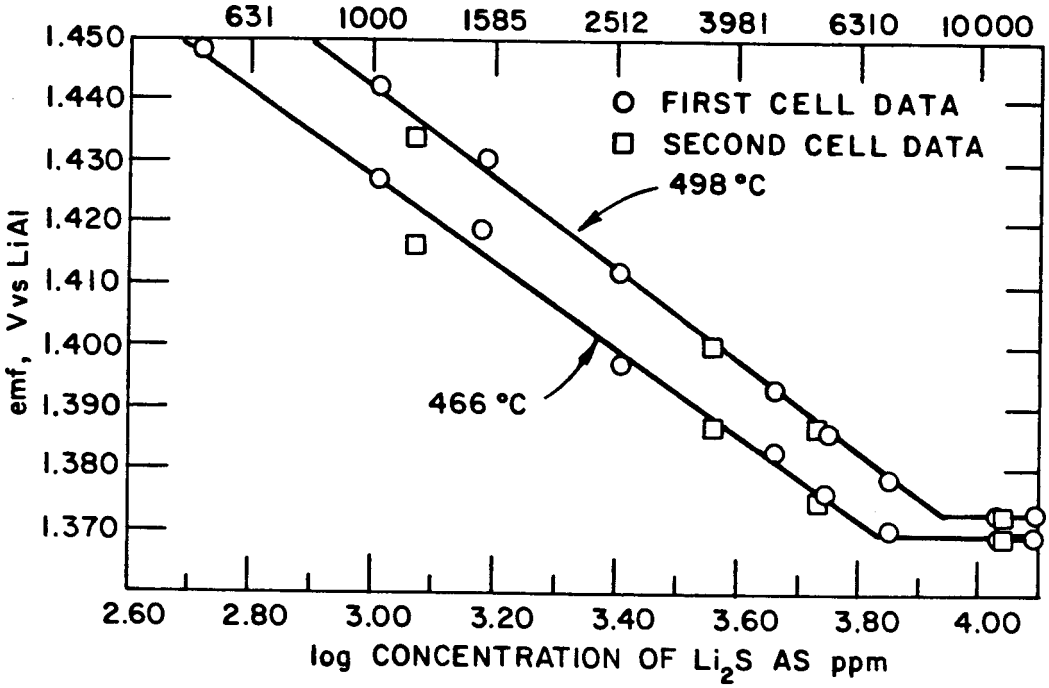

Fig. 16. Emf of Li-Al/Ni_3S_2 Couple vs. Li_2S Concentration in LiF-LiCl-LiBr Electrolyte

The measured solubility values agree well with those predicted from thermodynamic calculations* (6350 ppm at 466 °C and 8775 ppm at 480 °C). In making these thermodynamic calculations, the known solubility values of Li_2S in LiCl-KCl eutectic are used as the starting point. The activity of Li_2S is then calculated, as are changes in the composition of the electrolyte from LiCl-KCl to LiF-LiCl-LiBr electrolyte.

The horizontal portions of the curves in Fig. 16 yield the emf of the Li-Al/Ni_3S_2 couple in electrolyte saturated with Li_2S at 466 and 498 °C. In order to establish the emf vs. temperature curve for the Li-Al/Ni_3S_2 couple in Li_2S-saturated electrolyte, additional emf data were obtained in the temperature region of 462 to 520 °C. The experimental points resulting from these measurements, as well as those at 466 and 498 °C, are shown in Fig. 17. A linear regression analysis of the data shown in this figure was made, and the data were fit by the equation:

$$E(mV) = 1.365 + 0.092T(°C) \qquad (4)$$

The emf data obtained in this electrolyte saturated with Li_2S compare well with those obtained in different electrolytes; this comparison is made at temperatures of 400, 450, and 500 °C. The data in Table 3 clearly indicate that the emf of the Li-Al/Ni_3S_2 couple for a given Li_2S concentration is unaffected by electrolyte composition. This excellent agreement is consistent with the x-ray diffraction findings that Ni_3S_2 is the only nickel sulfide phase formed for the different electrolyte compositions tested.

*Performed by M. L. Saboungi, ANL.

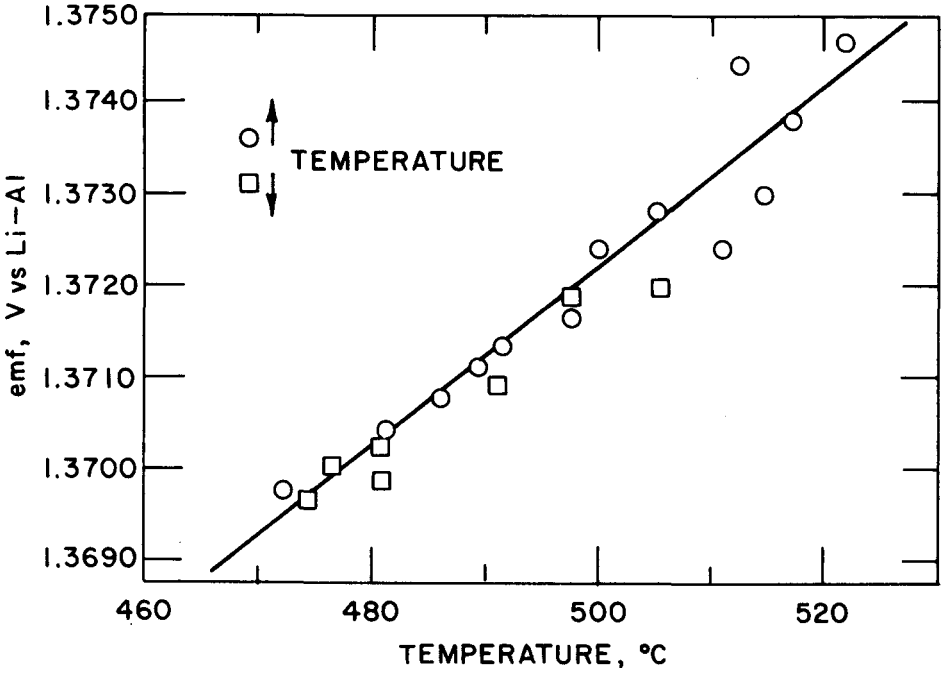

Fig. 17. Emf vs. Temperature Curve for the Li-Al/Ni_3S_2 Couple in LiF-LiCl-LiBr Saturated with Li_2S (circles were obtained when temperature was increased, squares when it was decreased)

Table 3. Emf Data for the Li-Al/Ni_3S_2 Couple in Different Electrolytes Saturated with Li_2S

	Emf, V vs. Li-Al		
Electrolyte (composition in mol %)	400 °C	450 °C	500 °C
LiCl-KCl (58.2-41.8)	1.3647	1.3688	1.3729
LiCl-KCl (49.1-50.9)	1.3648	1.3682	1.3715
LiCl-KCl (69.6-30.4)	1.3651	1.3688	1.3724
LiF-LiCl-LiBr (22-31-47)	1.3628	1.3675	1.3721

The emf data in Table 3 were used to calculate the free energy of formation of Ni_3S_2 at 700 K. For this calculation, the overall cell reaction is

$$4LiAl + Ni_3S_2 \leftrightarrow 2Li_2S + 3Ni + 4Al \qquad (5)$$

and the available thermochemical data for Li_2S and LiAl were used.[8,9] This calculation yields a free energy value of -196.73 kJ/mol, which is in excellent agreement with the reported value of -195.23 kJ/mol.[10]

C. Hot-Cell Microscope Studies of Li-Al and Li-Si Electrodes
(A. K. Fischer and D. R. Vissers)

To study processes involved in the morphological changes of the Li-Al and Li-Si electrodes, microscopic observations were made on functioning electroactive Li-Al and Li-Si structures. The *in situ* technique developed for these studies uses a cell with a quartz viewing window that is out of contact with electrolyte and is protected from condensing vapor during nonviewing periods by a shutter. Figure 18 is a photograph of the complete apparatus, showing the American Optical Stereostar Model 590X microscope and hot-stage cell.

Fig. 18. Hot-Cell Microscope Apparatus

The hot cell used working electrodes of either cast aluminum or a silicon block or powder; the counter and reference electrodes contained a powdered α-Al + β-LiAl. Consequently, all voltages cited in this work are relative to α-Al + β-LiAl. To perform the experiments, the cell was loaded with its electrodes and electrolyte in a high-purity helium-atmosphere glove box. The assembled cell was gas-tight and contained the glove box atmosphere. For the electrochemical operations and visual observations, the cell was then transferred from the glove box to a bench-top furnace. A slightly positive pressure of the inert atmosphere was maintained in the cell with an inert gas supply system.

1. Cast Aluminum Electrode Studies

The working electrode in these studies was cast in a stainless steel cup. The first electrode in this series contained 510 mg of aluminum and had

an area of 0.98 cm^2. This electrode was charged initially with lithium at 20 mA/cm^2 to a voltage cutoff of 22 mV (IR-free). Gas bubbles evolved from the surface when the experiment was started, and the surface appeared dimpled within the first 10 min. As deposition proceeded, the surface became gray and dark nodular spots appeared. The reaction product at the edges rose as a ridge, and appeared spongy. After the first discharge, in which 64% of the initially charged lithium had been removed from the electrode, the electrode was recharged. The cutoff of the second charge was -72 mV (IR-free), and nearly ten times as much lithium was deposited as in the first charge. During this charge, particles flaked off the surface. Tentacular roughness on the edges from the reaction product disk tended to break off easily, and the fragments drifted away into the electrolyte. Overall, the reaction-product disk appeared coherent, despite the loss of small particles. It protruded well above the stainless steel cup and broke through the electrolyte surface. This upward growth resulted from the volume changes associated with the formation of β-LiAl from α-Al.

A similar experiment with a cast aluminum-block electrode (1.63 g Al, 1.12 cm^2) was performed without any attempt to cycle. In this experiment, lithium was deposited to a higher cutoff potential, -200 mV. In the early stages, current densities of 18, 45, and 67 mA/cm^2 were used. Within 5 min at 18 mA/cm^2, a visible ridge, with cracks, developed on the circumference of the disk. After further growth at 45 mA/cm^2, this material appeared granular, but remained coherent when the furnace and cell were deliberately vibrated. In contrast, after the final high-current, high-overpotential portion was over, fine gray powdery material floated on the electrolyte and was heaped alongside the electrode. In the last stages of this experiment, the nominal current density was approximately 100 to 150 mA/cm^2, depending on how much of the expanded disk protruded above the electrolyte.

In a third experiment, a 310-mg aluminum-block electrode covered with a screen was used to examine a condition corresponding more closely to that in a developmental cell in which screens cover the electrode faces; the particular intent was to seek information on morphological events at the screen/electrode interface. The reaction depth within the aluminum cylinder was uneven, because the electrode was partially immersed and was tilted. During the first charge cycle, which proceeded in 10 mA increments of increasing current from 10 to 80 mA to a cutoff of -110 mV (IR-free), expansion of the electrode ruptured the screen. In the first discharge, where an electrode potential of +62 mV was reached, the edge of the Li-Al disk became roughened and scalloped, but there was no fragmentation of material. Subsequent charges and discharges (7-1/2 cycles) proceeded to final electrode potentials of -200 mV and 62 mV. Early in the second charge, the edge of the disk showed protrusive strands and some separation of these features was observed. At the end of this charge, granular reaction product in the main electrode area had begun to grow around the ends of the screen wires. In later charges, considerable amounts of Li-Al reaction product were seen separating from the submerged portion of the electrode and moving past the ruptured screen. A pile of this material accumulated on the bottom of the vessel, under the electrode. At the end of the fifth charge, fine, drifting Li-Al material almost covered the screen. Coverage was complete in the lower region of the screen at the end of the experiment.

2. Li-Si Electrode Studies

To investigate the processes involved in the morphological development of the Li-Si electrode, a powder electrode containing 55.1 mg of silicon (see Fig. 19A) was charged at a constant current of 20 mA. During the early portion of the first charge, where $Li_{1.71}Si$ was being formed, the material in a sharp zone next to the screen was being displaced upward by the expanding reaction product (Fig. 19B). As the reaction progressed, the electrode cavity was slowly filled with the expanding electrode bed (Fig. 19C). By the end of the Si + $Li_{1.71}Si$ plateau, the particle bed was nearly level with the top of the cavity. A mound formed during the charge process on the next plateau, $Li_{1.71}Si$ + $Li_{2.33}Si$, as illustrated in Fig. 19D. Particles on the side of the mound remained in place during vibration. The electrode potential at this point was -1.18 mV.

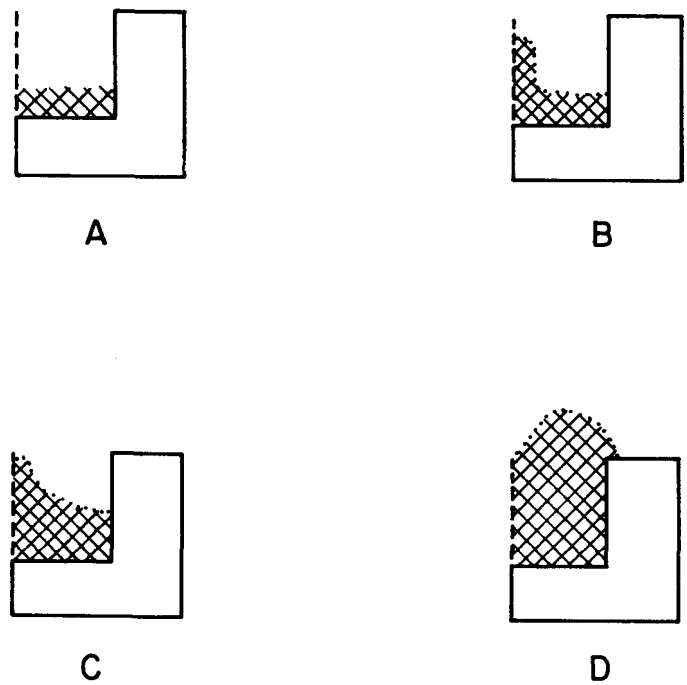

Fig. 19. Schematic of Cross-Sectional Side View of Reaction Product Distribution Progression in Silicon Powder Electrode

After a discharge cycle to -6 mV, the electrode was recharged. During this charge, a new plateau was reached at a potential of -142 mV, corresponding to the two-phase system $Li_{2.33}$-$Li_{3.25}Si$. After an overnight, open-circuit delay, charging was resumed and the -142 mV plateau was reestablished, during which time considerable particulate matter, resembling flakes of Li-Si reaction product, could be seen circulating in the electrolyte around the electrode. Next, the electrode was charged to the $Li_{3.25}Si$-$Li_{4.4}Si$ plateau at -251 mV; again, many flakes of Li-Si reaction product could be seen entering

the electrolyte. During the last discharge, the potential trace went through a series of breaks of slumping plateaus, and ended in the $Li_{1.71}Si$ single-phase field, although the coulomb count suggested a possibly higher residual lithium content. These results suggest that the internal diffusion kinetics are rather slow, or that self-discharge might have taken place.

In the second Li-Si electrode study, a 70-mg cube of silicon was brazed in copper powder with silver solder in a stainless steel cup. This electrode is the only one of this series that was charged potentiostatically. There were no discharges. Estimated current densities ranged from 15 to 515 mA/cm^2. Initial deposition at +30 mV (in the $Li_{1.71}Si$-Si two-phase region) resulted in some cracking, accompanied by growth of a rim at the edges of the silicon surface. In a series of depositions at successively more negative potential steps, the rim became lava-like in appearance, showing cracking but no fragmentation. During this time, the block could be seen growing upward. The most negative deposition potential was -100 mV, which is in the $Li_{2.33}Si$-$Li_{1.71}Si$ two-phase field. No powder formation or separation of particles or fragments was observed at any time in the experiment. In the final period of the charge, as the coherent electrode grew upward, it also pulled upward some of the casting matrix around its base. Post-experiment metallographic examination revealed only slight indications that lithium had deposited and reacted at the surface of the copper-silver solder casting matrix.

The results of these different studies clearly indicate that the hot-cell microscope technique can be used to investigate processes associated with morphological changes of electrodes operated in molten salt. The studies indicate, for example, that (1) gases are released when lithium is first charged into the α-Al (these gases may be associated with absorbed helium or H_2O), (2) the morphology of the electrode material formed from a single charge cycle tends to be coherent, (3) the quantity of fines generated in the electrode during cycling appears to be related to the overpotential to which the electrode was driven during the charge cycles, and (4) the lithium-reaction front into the silicon powder electrode tends to be focused initially at the front face of the electrode, as is predicted theoretically for electrodes in which the electronic conductivity of the electrode material is greater than the ionic conductivity of the electrolyte.[11]

D. Electrochemical Engineering and Cell Design Studies

(F. J. Martino, W. E. Moore,* and E. C. Gay)

The purpose of this task is to develop a computer model that will correlate the effects on performance of design and operating variables observed in small-scale experimental cells; these data will be used to provide a projection of the performance of full-scale cells.

1. Operation of Experimental Cells

The performance of engineering-scale cells can be predicted by means of computer modeling, using input data from small-scale experimental bicells (100 cm^2, 20-35 Ah). Such cells are being operated, using compact, cell

*Resident Student Associate, Illinois Institute of Technology, Chicago, IL.

designs with lightweight hardware. Initial studies have been focused on the effects on cell performance of design parameters, e.g., electrode thickness, loading density, negative-to-positive capacity ratio, electrolyte and electrode compositions. In addition, the effect of increased lithium concentration and activity on the separator performance will be determined. Operating variables include discharge and charge current density, cut-off voltages, and temperature. Performance measurements include utilization, peak power, cycle life, capacity decline with cycling, and 15-second steady-state and transient polarization (ASR values) measurements at different states of charge.

A factorial matrix of the major variables in the present study is presented in Table 4. Additional cells will be operated under modified conditions (e.g., charge rate, charge voltage cutoff) to determine the effects of these variables on performance.

Table 4. Variables for Experimental Cell Study

Experiment No.	Positive Electrode Thickness, cm	Negative Electrode Loading Density, Ah/cm^3	Negative-to-Positive Capacity Ratio
1	0.3	0.8	1.0
2	0.4	0.8	1.0
3	0.3	0.9	1.0
4	0.4	0.9	1.0
5	0.3	0.8	1.2
6	0.4	0.8	1.2
7	0.3	0.9	1.2
8	0.4	0.9	1.2

a. Baseline Li-Al/FeS Cells

To provide baseline reference data for cells using advanced active materials (i.e., Li-Si, Li-Al-M, FeS_2, NiS_2), Li-Al/FeS cells with a lightweight, high-power design were tested. Both the positive and negative electrodes had front-face current collectors of perforated iron sheet (0.25-mm thickness, 45% open area, 0.97-mm ID hole size) with nickel terminals inserted into the 8.7 cm-high by 6.3 cm-wide electrodes. Boron nitride felt was used as the electrode separator in all the test cells.

Design variables for the first five cells tested (MNU-1 to -5) are shown in Table 5. The cells were designed to measure the effect on performance of negative electrode fabrication method (pressed vs. slurried), MNU-1 and -2; negative electrode loading density, MNU-2 and -3; electrode thickness, MNU-2 and -4; and electrode orientation, MNU-4 and -5. Operating conditions for these cells included deep-discharge cycling to 0.9-V cutoff and a charge current density of 37 mA/cm^2 to a 1.65-V cutoff. The cell operating temperature was 465°C.

A summary of the performance for the five test cells is presented in Table 6. The results were as follows: (1) Cell MNU-2 produced the highest utilization (83% at the 3-h discharge rate) and peak power densities

Table 5. Li-Al/FeS Bicell Test Parameters

	MNU-1	MNU-2	MNU-3	MNU-4[d]	MNU-5[d]
Positive Electrode[a]					
Thickness, cm	0.31	0.31	0.31	0.41	0.41
Theor. Cap., Ah	21.6	21.6	21.6	28.7	28.7
Electrolyte vol. fract.	0.51	0.51	0.51	0.51	0.51
Load. Dens., Ah/cm^3	1.4	1.4	1.4	1.4	1.4
Negative Electrode[b]					
Thickness,[c] cm	0.32	0.32	0.29	0.43	0.43
Theor. Cap., Ah	26.0	26.0	26.0	34.4	34.4
Electrolyte vol. fract.	0.45	0.45	0.39	0.46	0.46
Load. Dens., Ah/cm^3	0.80	0.80	0.90	0.80	0.80
Negative/Positive Ratio	1.2	1.2	1.2	1.2	1.2
Electrolyte	54 wt % LiCl-KCl				

[a]All positive electrodes are pressed; 100 cm^2 electrode area.

[b]All negative electrodes are slurry-formed except for those of cell MNU-1 (pressed).

[c]Half-electrode thickness.

[d]The electrode orientation for cell MNU-4 was 8.7-cm height by 6.3-cm width; for cell MNU-5, 6.3-cm height by 8.7-cm width.

Table 6. Performance Summary of Small-Scale (100 cm^2) Li-Al/FeS Bicells

	MNU-1	MNU-2	MNU-3	MNU-4	MNU-5
Positive Util.,[a] %					
6-h rate	86	87	75.5	76	75
3-h rate	83.5	83	72.5	72.5	73
1-h rate	70	70	57	57	58
Area-Specific Resistance,[b] Ω-cm^2					
3% DOD	0.50	0.49	0.63	0.66	0.62
50% DOD	0.54	0.53	0.66	0.66	0.69
Peak Power,[c] W					
3% DOD	90	93	85	78	79
50% DOD	65	61	43	60	49
Deep Discharge Cycles[d]	253	220	247	120	60

[a]Approximately 35, 60, 150 mA/cm^2, respectively; cycled between 0.9 and 1.65 V.

[b]Determined by 1-s current interruption.

[c]Taken with 15-s current pulse to ~125 A.

[d]Based on 3-h discharge rate (~60 mA/cm^2).

(0.92 and 0.63 W/cm^2 at 3% and 50% depth of discharge, respectively); (2) pressed or slurry-formed negative electrodes performed equally well; (3) thick electrodes and high negative-electrode loading densities resulted in the lowest utilizations, and (4) electrode orientation (8.7-cm height vs. 6.3-cm height) had little effect on performance.

b. Li-Al/FeS_2 Cells

Experimental small-scale (100-cm^2, 30-Ah) Li-Al/FeS_2 bicells are being tested to determine cell performance as a function of selected variables. The variables of interest include active material composition, negative-to-positive capacity ratio, electrode loading density, electrolyte composition, and electrode thickness. These cells are being operated to determine their voltage, capacity density and capacity stability, polarization, and cycle life.

The entire current-collector assembly for the positive electrode is fabricated from molybdenum. At present, the most reliable and easily reproduced current-collector design is that of a welded center sheet/rod with molybdenum screen at the electrode faces. The negative electrode current collector is the same as that used in the series of tests on small-scale LiAl/FeS cells. It consists of a mechanically perforated iron sheet attached to an iron tray to which nickel terminals have been brazed and welded. The BN felt separator was treated with $LiAlCl_4$, an electrolyte wetting agent. The electrolyte was LiCl-KCl eutectic. The negative electrodes were 53 at. % Li-Al.

Eight Li-Al/FeS_2 cells are now in operation; six of them are described in Table 7. The first series of cells was limited to a 1.95-V charge cutoff and a charge current density of 16 mA/cm^2 (8- to 10-h charge rate). A review of previous Li-Al/FeS_2 cell tests showed a possible improvement in capacity retention with cycling under these conditions.

Table 7. Small-Scale (100 cm^2) Li-Al/FeS_2 Bicell Test Parameters[a]

	MLBL-1	MLBL-2	MLBL-5	MLBL-6	MLBL-7	MLBL-8
Positive Electrode[b]						
Thickness, cm	0.30	0.40	0.30	0.40	0.30	0.40
Theor. Cap., Ah	25.2	33.3	25.2	33.3	25.2	33.3
Negative Electrode						
Thickness,[c] cm	0.29	0.39	0.36	0.47	0.32	0.42
Theor. Cap., Ah	25.2	33.3	30.1	40.1	30.1	40.1
Electrolyte vol. fract.	0.445	0.445	0.445	0.446	0.375	0.376
Load. Dens., Ah/cm^3	0.80	0.80	0.80	0.80	0.90	0.90
Negative/Positive Ratio	1.0	1.0	1.2	1.2	1.2	1.2

[a]LiCl-KCl eutectic electrolyte.

[b]Volume fraction electrolyte was 0.651; loading density was 1.55 Ah/cm^3.

[c]Half-electrode thickness.

A summary of the Li-Al/FeS_2 cell performance is presented in Table 8. Cells MLBL-1 and MLBL-5 were identical, except for the difference in the negative-to-positive capacity ratio, as were Cells MLBL-2 and MLBL-6. There is a slight improvement in the utilization for cells having a negative-to-positive capacity ratio greater than one. Cells MLBL-5 and MLBL-7 were

Table 8. Performance Summary of Small-Scale (100 cm^2) Li-Al/FeS_2 Bicells

Cell No. MLBL-	1	2	5	6	7	8
Positive Util.,[a] %						
8-h rate	-	63	70	65	67.5	62
3-h rate	59	49	60	54.5	59	48
1-h rate	44	36	48	45	40	36
Area-Specific Resistance,[b] Ω-cm^2						
3% DOD	-	1.11	1.20	1.10	1.14	1.24
50% DOD	-	0.87	1.05	1.05	1.01	1.26
Peak Power,[c] W						
3% DOD	-	69	65	69	72	55
50% DOD	-	56	40	40	35	38
Cycle Life Data[d]						
Deep Discharges	>91	>64	>145	>125	>135	>150
Capacity Decline, %/cycle	0	0	<0.01	<0.01	<0.01	<0.01

[a]Approximately 35, 60, 150 mA/cm^2, in the same order; cycled between 0.9 and 1.95 V.

[b]Determined by 1-s current interruption.

[c]Taken with 15-s current pulse to ~100 A.

[d]Based on 3-h discharge rate (~60 mA/cm^2).

identical, except for the difference in negative electrode loading density; the same applies to Cells MLBL-6 and MLBL-8. The cells having a negative electrode loading density of 0.8 Ah/cm^3 showed slightly higher utilization than those cells with a loading density of 0.9 Ah/cm^3. All the cells showed good capacity retention with cycling. The capacity-decline rates were 0 to 0.01% per cycle over 64 to 150 cycles. Examples of stable capacity for these cells are shown in Figs. 20 and 21. The low capacity-decline rates are a significant improvement over those for Li-Al/FeS_2 cells tested previously and shown in Table 9. The operating conditions for these earlier cells are shown in Table 10. The best performers among these cells were charged at lower rates and to lower charge voltage cutoffs, but there were a number of exceptions.

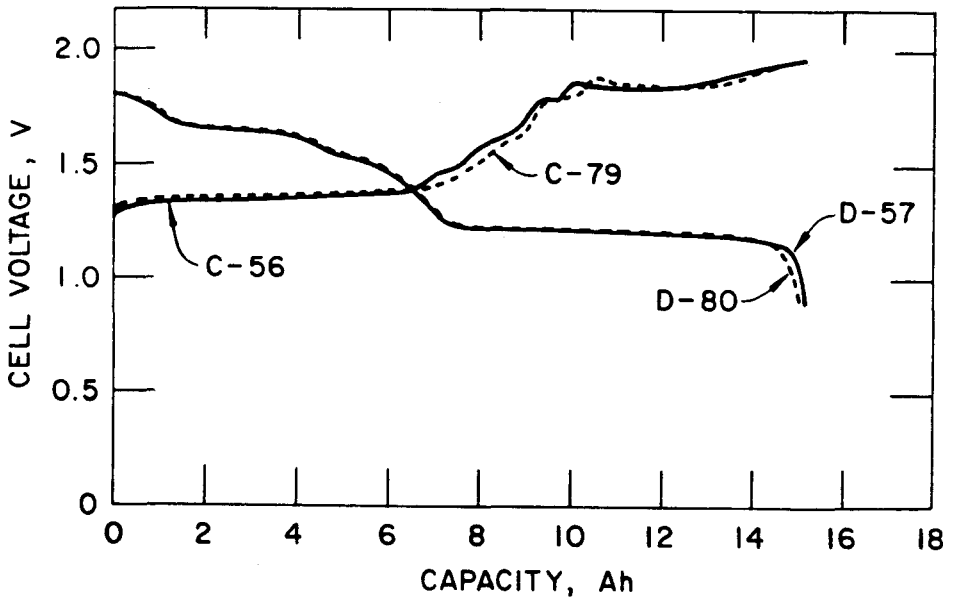

Fig. 20. Voltage vs. Capacity for Li-Al/FeS_2 Cell MLBL-5 (theoretical capcity, 25.2 Ah; temperature, 427°C; discharge current density, 52 mA/cm^2; charge current density, 16 mA/cm^2)

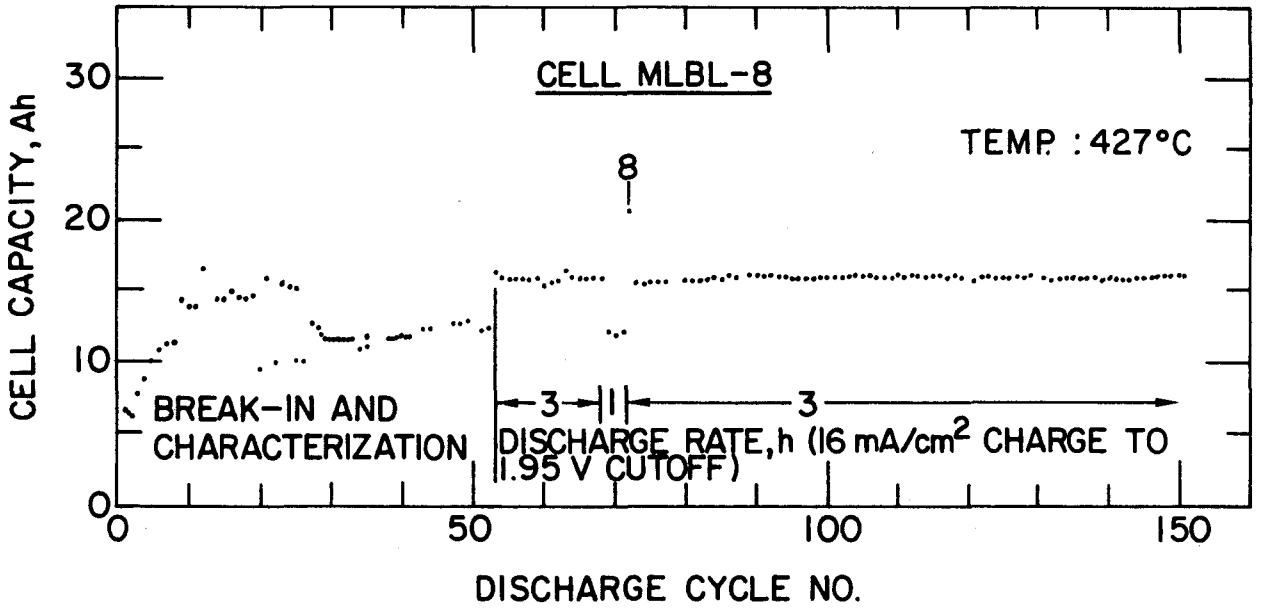

Fig. 21. Cycle-Life Summary for Cell MLBL-8

Table 9. Li-Al/FeS_2 Bicells Tested at ANL during 1977 and 1978

Cell No.	Theor. Cap.,[a] Ah	Specific Energy (C/4), Wh/kg	Cycles Tested	Neg./Pos. Capacity Ratio	Specific Power (50% SOC), W/kg	Percent Capacity Decline Per Cycle
M-4	165	87	292	0.6	90	0.14
M-7	194	97	137	1.2	125	0.26
2A5	68.8	65.7	310	1.0	55	0.13
2B6	155	75.4	225	1.0	[b]	0.22
2B8	155	78.7	532	1.0	[b]	0.06
I8H-040	117	76.5	420	1.3	[b]	0.04
G-04-003	207	49.4	325	1.3	[b]	0.10
I8F-17	170	43.9	250	1.0	[b]	0.12
YF-1	74.6	[b]	663	0.8	[b]	0.03

[a]Capacity of the limiting electrode.

[b]Data were not available.

c. Li-Si/FeS_2 Cells

In response to emphasis on alternative negative-electrode active materials and compositions of higher gravimetric and volumetric energy densities, a $Li_{3.25}$ Si/FeS_2 cell was constructed. The active material composition for this cell was similar to that used in the monocell reported in Section II.A.4 of this report. The cell used in the present study contained lightweight hardware, including a molybdenum positive-electrode current collector identical to that used in the LiAl/FeS_2 cells reported earlier. The nickel negative electrode current collector included a nickel Retimet substrate, and boron nitride felt separator and LiCl-KCl eutectic were also used in the cell.

The positive electrode was fabricated in the partially discharged state by mixing FeS_2 and X-phase, and the negative electrode consisted of Li_2Si powder (vibrationally loaded into the nickel Retimet substrate). The fully charged cell should be $Li_{3.25}$ Si/FeS_2, with 20% excess capacity in the negative electrode (25 Ah, positive; 30 Ah, negative). The charged cell was virtually identical to its LiAl/FeS_2 counterpart (MLBL-5), aside from the presence of the Retimet substrate and the composition of the negative electrode active material. This cell (designated MLBLS-1) is undergoing characterization cycling under operating conditions similar to those used in the testing of the Li-Al/FeS_2 cells (i.e., 1.95-V charge cutoff, 16-mA/cm charge current density, 427°C operating temperature). Comparison of the Li-Si/FeS_2

Table 10. Operating Conditions for Li-Al/FeS_2 Cells Tested at ANL during 1977 and 1978

Cell No.	Cell Operating Temp., °C	Coulombic Efficiency at End of Testing, °C	Cycles with >95% Coulombic Efficiency	Charge Cut-off Voltage,[a] V	Cell Resistance, mΩ	Initial Vol. Fract. Salt in Positive
M-4	450	79.4	145	2.2	3.2	0.60
M-7	450	82.2	25	2.2	2.4	0.60
2A5	430	91.2	190	2.0-2.2	8.5	0.76
2B6	430	82.7	200	1.9-2.1	b	0.75
2B8	435	63.7	300	2.0	b	0.75
18H-040	415	90.6	375	2.2	b	0.61
G-04-003	430	76.1	100	1.95	b	0.60
18F-17	425	100	250	2.0-2.2	b	0.77
YF-1	450	74.3	350	2.1	b	c

[a]All of the cells were charged at the 8-h rate except Cell YF-1, which used current-limited constant-voltage (2.1 V) charging over a 5-h period. All of the cells were discharged at the 4-h rate to a 0.9-V or 1.0-V cutoff.

[b]Data were not available.

[c]Hastelloy B foam used in the positive electrode; porosity not available.

cells and Li-Al/FeS_2 cells indicates some improvement in overall cell performance with the Li-Si electrode. For example, the positive electrode utilization at the 3-h discharge rate (53 mA/cm^2) was improved approximately 6% and the specific energy by 6%; the upper voltage plateau was extended from 7.5 Ah (Li-Al) to 11 Ah (Li-Si), which is about 50% greater than the range for the Li-Al/FeS_2 cell. The average cell voltage remained at approximately 1.40 V, because the second voltage plateau is lower for the Li-Si/FeS_2 cell than for the Li-Al/FeS_2 cell. A typical 3-h discharge voltage profile for the Li-Si/FeS_2 and Li-Al/FeS_2 cells is presented in Fig. 22. The increased capacity of the upper plateau in the Li-Si/FeS_2 cell is expected to provide improved power output through 50% DOD.

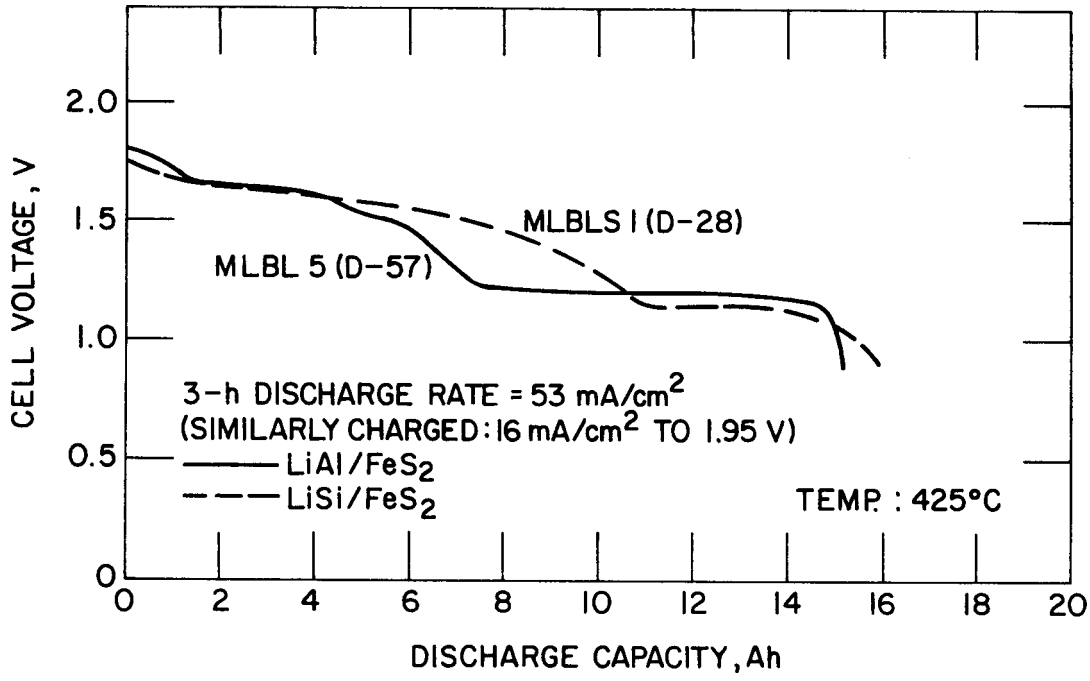

Fig. 22. Comparison of Discharge Voltages for Li-Al and Li-Si Electrodes

Cycling of the Li-Si/FeS_2 cell through 100 deep discharge cycles showed poor capacity retention with cycling. The capacity-decline rate was 0.20% per cycle. In the post-test examination of the cell, particular attention will be given to possible high rates of corrosion of the nickel current collector by the Li-Si, which would account for the high rate of capacity decline.

2. Computer Program for Advanced-Cell Design Studies

Important factors in the design of batteries for electric-vehicle propulsion include battery capacity, specific energy, specific power, and power-to-energy ratio. One approach to investigation of power and energy trade-offs is to vary the size of the current collector, interelectrode connectors, terminals, and thickness of the electrodes in the cell. A computer program for the design and optimization of Li-alloy/iron sulfide cells has been developed with the capability of calculating voltage losses across all of the current-carrying elements of the cell. These losses can be distributed as desired across the electrode current collectors, interelectrode connectors, and cell terminals. Input to the program includes the usable capacity at a given discharge rate and the power-to-energy ratio. The program was developed on the basis of data from small-scale experimental cells that define the effects of design and operating variables on performance. Ohmically and electrochemically related bed resistances are calculated from equations derived from ASR measurements taken in electrode-polarization studies. On the basis of these data, the program projects the performance of full-scale cells for advanced systems.

A modular approach was used in the development of the computer design program. This approach provides flexibility in changing active material and electrolyte compositions, type of separator, type of current collector, cell shape, and cell configuration. The variables are changed by merely replacing a data pack in the program.

An approach proposed by P. A. Nelson[12] was used to develop equations relating the ARS to cell-design variables. Resistivity of the electrode bed is equal to ASR divided by the electrode thickness. Based on considerations of limiting conditions and theory:

$$R_t = \frac{a}{(1 - U)(1 - e_f^*)\ V} \tag{6}$$

where R_t = transfer resistance of the electrode

U = electrode utilization

V = electrode volume

e_f^* = volume fraction electrolyte in the electrode in the charged state

a = constant

Also,

$$R_i = \frac{\delta_e T^2}{2V e_f^*} \tag{7}$$

where R_i = ionic resistance

δ_e = electrolyte resistivity

T = electrode thickness

An analysis of the ASR data shown in Table 11 for Li-Al and FeS electrodes provided the following equations. For the FeS electrode,

$$ASR_{15s} = \frac{0.0226}{(1 - U_p)(1 - e_f^*)T_p} \tag{8}$$

where ASR_{15s} = 15-second area specific resistance

U_p = positive electrode utilization

T_p = positive electrode thickness

Table 11. Area-Specific Resistance[a] of Li-Al and FeS Electrodes Based on the LCS-Series Cells

	LCS-2				LCS-3		LCS-4			
	Pos.	Neg.	Pos.	Neg.	Pos.	Neg.	Pos.	Neg.	Pos.	Neg.
Current Dens.,[b] mA/cm^2	43	43	271	271	40	40	60	60	271	271
ASR_{15s}, mΩ-cm^2	480	70	620	120	410	70	250	60	380	120
Electrode Half-thickness, cm	0.16	0.30	0.16	0.30	0.26	0.49	0.26	0.49	0.26	0.49
Loading Density, kC/cm^2	5.0	3.5	5.0	3.5	4.0	2.8	5.0	3.5	5.0	3.5

[a]The data shown in this table are for 50% state of charge and were provided by L. Redey based on studies discussed in Section II.A of this report.

[b]Electrode area was 106.9 cm^2.

For the Li-Al electrode,

$$ASR_{15s} = 0.051/(1 - U_n) \quad (9)$$

where U_n = negative electrode utilization. Figure 23 shows the extremely good correlation achieved with Eqs. 8 and 9 for the ASR of the LCS-series cells over nearly the entire discharge. The largest deviations occurred at the end of discharge, where very high polarization was observed in the positive electrode. Further work in this area will focus on the development of equations to calculate ASR values for FeS_2 electrodes.

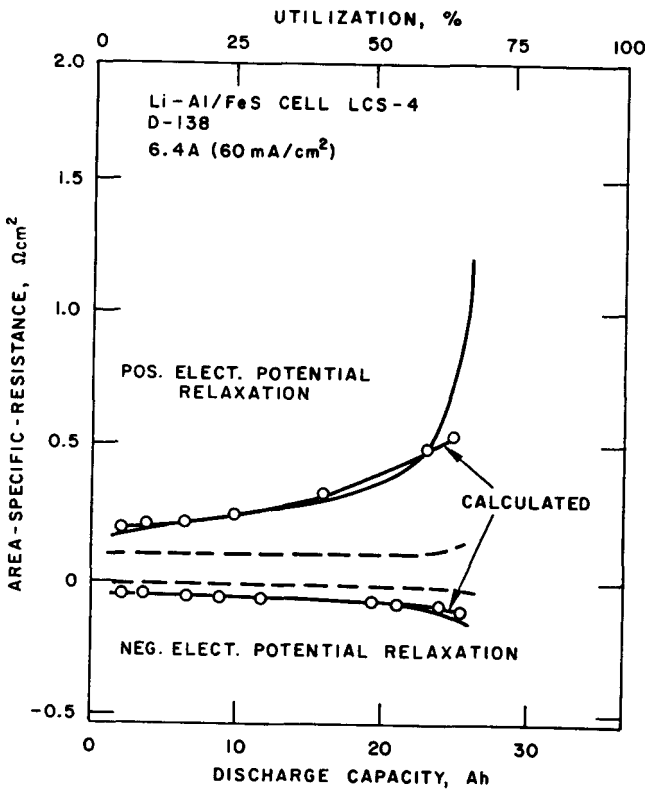

Fig. 23.

Calculated and Measured ASR for Li-Al/FeS Cell

An examination of the proposed equations for the electrode-bed resistance, Eqs. 6 and 7, and the equations derived from the multiple regression analysis of the ASR data showed that the variables in Eq. 6 for the transfer resistance were most similar to the form of the equations developed for ASR. The form of Eq. 6 and the equation for the ASR of the FeS electrode are equivalent, recognizing that the resistance is equal to ASR divided by the electrode area.

Comparisons have been made between the calculated and measured performance of a number of Li-Al/FeS cells. Included are the experimental baseline-data Cells MNU-2, -3, and -4 (Section II.D.1 of this report); Cell LCMP-17, which achieved the highest combination of specific energy and specific power for a Li-Al/FeS cell tested to date (Section III.B.3); and Eagle-Picher Cell 176 (Section III.A.3), which had nearly 400-Ah capacity. The calculated and measured specific energy and specific power values are presented in Figs. 24 and 25. This comparison shows good agreement between the measured and

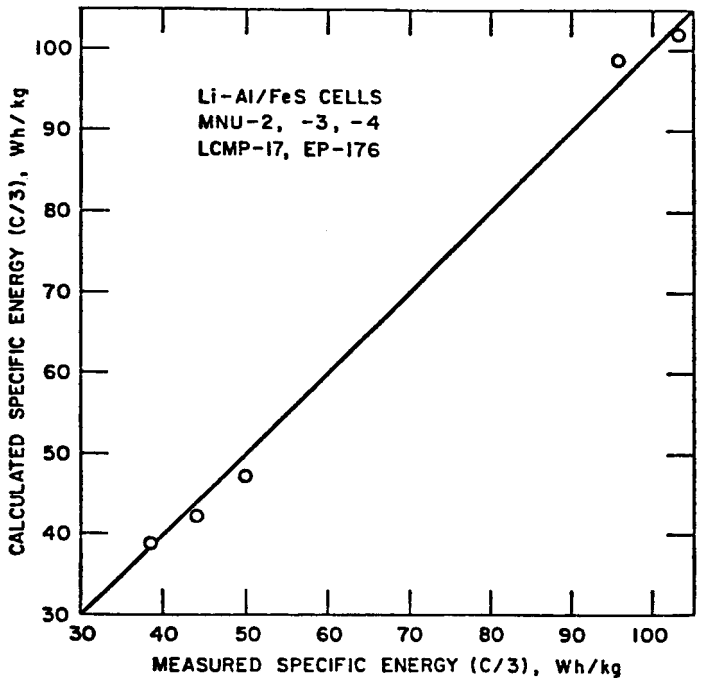

Fig. 24. Calculated vs. Measured Specific Energies for Selected Li-Al/FeS Cells

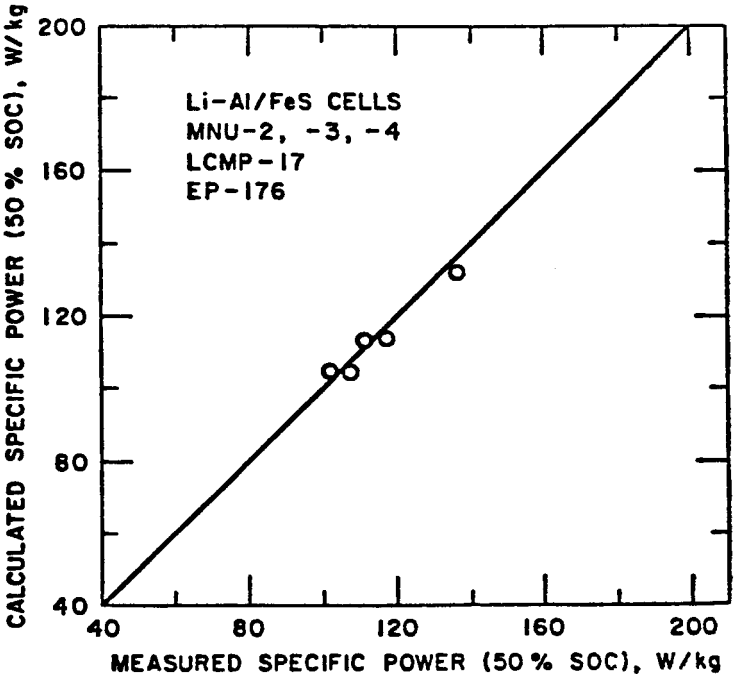

Fig. 25. Calculated vs. Measured Specific Power Values for Selected Li-Al/FeS Cells

calculated values. A more detailed comparison between as-fabricated cells (MNU-2 and EP 176) and calculated component designs is shown in Tables 12 and 13. These results show good agreement between the calculated and as-fabricated components, as well as agreement between the measured and calculated performances.

Table 12. Design and Performance Correlation for Cell MNU-2 (fabricated by ANL)

	Cell MNU-2	Calculation from Computer Model
Positive Electrode		
Size, cm x cm	6.2 x 8.7	5.9 x 8.7
Theor. Capacity, Ah	21.6	21.6
Thickness, cm	0.31	0.31
FeS Weight, g	35.5	35.4
Active Material Loading Density, Ah/cm^3	1.4	1.4
No. of Parallel Electrodes	1	1
Electrode Utilization, %	83	83
Negative Electrodes		
Thickness, cm	0.64	0.66
53 at. % Li-Al Weight, g	29.9	30.8
Active Material Loading Density, Ah/cm^3	0.8	0.8
No. of Parallel Electrodes	2	2
Negative-to-Positive Capacity Ratio	1.2	1.2
Electrolyte Weight (54 wt % LiCl-KCl), g	134.2	136.3
Current Collector		
Perforated Particle Retainer Thickness, cm	0.025	0.026
Total Current-Collector Weight, g	113	100.2
Open Area Fraction of Perforated Plate	0.55	0.55
Terminal Diameter, cm	0.63	0.63
Cell Resistance, mΩ	5.6	7.4
Cell Housing		
Thickness, cm	0.063	0.063
Weight, g	80.8	99.3
Total Cell Weight, kg	0.52	0.51
Specific Energy (C/3), Wh/kg	43.8	42.2
Specific Power (50% DOD), W/kg	117	114
Power-to-Energy Ratio	2.7	2.7

Table 13. Design and Performance Correlation for EP Cell 176 (fabricated by Eagle-Picher)

	EP Cell 176	Calculation from Computer Model
Positive Electrode		
Size, cm x cm	18.4 x 17.5	18.7 x 17.5
Theor. Capacity, Ah	394.8	394.8
Thickness, cm	0.33	0.33
FeS Weight, g	647.2	647.2
Active Material Loading Density, Ah/cm^3	1.4 (1.36)[a]	1.3
No. of Parallel Electrodes	3	3
Electrode Utilization, %	91.5	91.5
Negative Electrodes		
Theor. Capacity, Ah	511.8	513
Thickness, cm	0.64	0.62
48 at. % Li-Al Weight, g	741.7	743.8
Active Material Loading Density, Ah/cm^3	0.93 (0.83)[a]	0.86
No. of Parallel Electrodes	4	4
Negative-to-Positive Capacity Ratio	1.3	1.3
Electrode Utilization, %	70.6	70.6
Electrolyte Weight (54 wt % LiCl-KCl), g	1350	1315.6
Current Collector		
Particle Retainer Thickness, cm	0.013	0. 012
Total Current-Collector Weight, g	1376	1030.5
Open Area Fraction of Particle Retainer	0.26	0.26
Terminal Diameter, cm	0.95	0.95
Cell Resistance, mΩ	0.86	0.93
Cell Housing		
Thickness, cm	0.046	0.046
Weight, g	590[b]	384[c]
Total Cell Weight, kg	4.793	4.408
Specific Energy (C/4), Wh/kg	93.9	98
Specific Power (50% DOD), W/kg	102	105
Power to Energy Ratio	1.06	1.06

[a]Value in parentheses includes volume of retainer frame at edge of electrode.

[b]Top of cell housing and feedthrough shell weight is 185 g.

[c]Weight with 185-g header would be 599 g.

E. Materials Research
(J. A. Smaga and J. E. Battles)

The reaction of the aluminum in the Li-Al alloy with the negative electrode hardware materials (nickel, low-carbon steel, and Type 304 stainless steel) results in the formation of a brittle, intermetallic reaction layer, which can reduce the conductivity of current collectors and decrease the strength of the electrode retainers. The reaction is twofold: galvanic deposition of aluminum onto the component surface and subsequent diffusion into the components. In separate experiments, the deposition and diffusion rates were measured to determine the rate-controlling mechanism. Additional diffusion experiments were conducted to evaluate candidate coating materials for the prevention of diffusion between aluminum and the substrate material.

1. Galvanic Deposition

Each galvanic deposition experiment was conducted in LiCl-KCl eutectic electrolyte in the temperature range of 470 to 530°C. The low-carbon steel (AISI 1008) electrode with a surface area of 6.5 cm^2 was electronically coupled, by a potentiostat, to an aluminum electrode of 32 cm^2 surface area. Once the circuit is closed, the cathodically controlled couple is immediately polarized to within 2 or 3 mV of the open-circuit potential for aluminum, and remains near that initial value during the experiment. The current shows a parabolic decay during the first one to three hours; after this initial phase, the current increases linearly until it stabilizes within a narrow range. The time to achieve a "steady-state" value ranged from 10 to 20 h, with tests at the lower temperature requiring the longer periods.

The steady-state current value was used to calculate a galvanic deposition rate, G, for each of the different test temperatures. These calculated rates were compared with the rates derived from measured weight gains of aluminum obtained in earlier tests in which the low-carbon steel/aluminum couple was immersed in molten LiCl-KCl electrolyte for 240 h.[13] The data from both types of experiments are represented graphically in Fig. 26. The data show that the temperature dependence of the deposition rate obeys an Arrhenius relationship:

$$G = G_o \exp(-Q/RT) \qquad (10)$$

where the activation energy, Q, is 21.4 $kcal \cdot mol^{-1}$, the gas constant, R, is 1.987 $cal \cdot mol^{-1} \cdot K^{-1}$, and the galvanic deposition rate constant, G_o, is 5.2×10^8 $mg \cdot cm^{-2} y^{-1}$ or 1.65×10^2 $g \cdot cm^{-2} \cdot s^{-1}$.

This current-monitoring technique provides estimates of aluminum deposition rates that are as reliable as those obtained from 240-h immersion tests but in a much shorter time. The data for a similar study of aluminum-nickel couples, although still incomplete, indicate that the deposition behavior is analogous to that described for low-carbon steel.

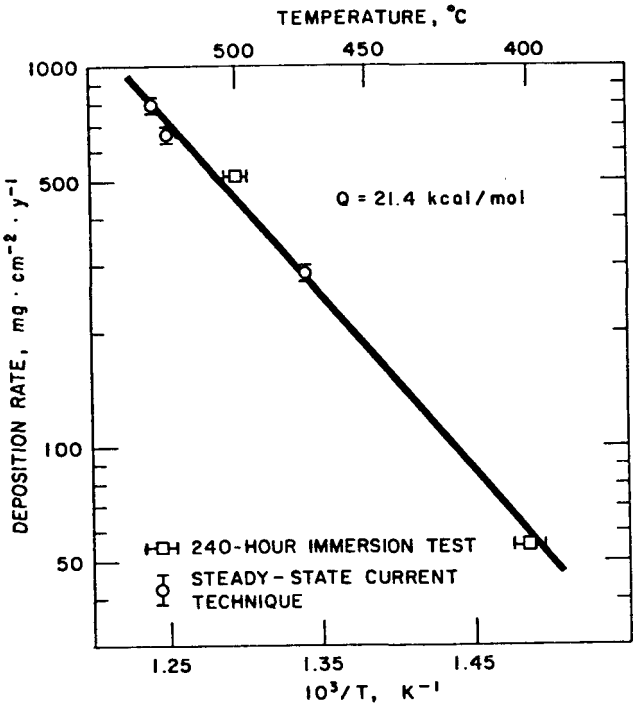

Fig. 26.

Temperature Dependence for the Galvanic Deposition of Aluminum onto Low-Carbon Steel

2. Aluminum Diffusion

Aluminum-diffusion experiments were conducted using a special holder assembly that supports the test specimen between sets of aluminum 1100 (99.0 +%) cylinders. For each experiment, the assembly was placed in a furnace well with an inert-gas atmosphere and heated at 475°C for 100, 500, or 1000 h. After testing, each diffusion couple was bonded in epoxy resin, sectioned in the longitudinal direction, and then prepared for optical and scanning electron microscopy (SEM) examination.

For the aluminum/low-carbon steel couples, the diffusion region consisted predominantly of a single-phase zone of $FeAl_3$.* For the aluminum/nickel couples, the diffusion region consisted of an inner zone of Ni_2Al_3 and an outer zone of $NiAl_3$. The diffusion region was thicker for the nickel couples than for the steel couples after equivalent time intervals, and was 105 to 110 μm thick for the former after 1000 h. Thickness measurements on the unaffected test metal were used to deduce the depth of penetration beyond the original interface. For both materials, approximately 25% of the diffusion-layer growth occurred at the expense of the test metal. For both materials, the reaction follows a parabolic growth rate. The diffusion coefficients are $3.4 \pm 3 \times 10^{-11}$ and $2.7 \pm 3 \times 10^{-11}$ $cm^2 \cdot s^{-1}$ for nickel and low-carbon steel, respectively.

*B. Tani, Analytical Chemistry Laboratory, ANL.

3. Rate-Controlling Mechanism

An analysis of the data from both the deposition and diffusion experiments for low-carbon steel indicated that the rate-controlling step for the overall aluminum reaction shifts from galvanic deposition to diffusion with time. At 475 °C, Eq. 10 predicts a deposition rate, G, of 9.1×10^{-9} g/cm^2·s. The thickness, x, of the deposited layer, allowing for conversion to $FeAl_3$, can be expressed as:

$$x = 1.67(G/\rho)t \qquad (11)$$

where t is the time in seconds, ρ is the density of $FeAl_3$, (3.8 g/cm^3), and 1.67 represents a combination of conversion constants needed to derive the weight of $FeAl_3$ formed from the deposited aluminum. The growth of the diffusion layer for low-carbon steel is governed by the equation:

$$x^2 = Dt \qquad (12)$$

where the diffusion coefficient, D, is 2.7×10^{-11} cm^2/s at 475 °C. Equations 11 and 12 are plotted in Fig. 27. At first, the overall aluminum reaction is controlled by the initially slower galvanic deposition, and it shows a linear dependence on time. However, once a certain transition time has been reached, the reaction is limited by diffusion, as indicated by the rate that follows a parabolic curve. Solving Eqs. 11 and 12 simultaneously gives a value of 19.1 days for the transition time. By this time the reaction layer is 66.7-μm thick.

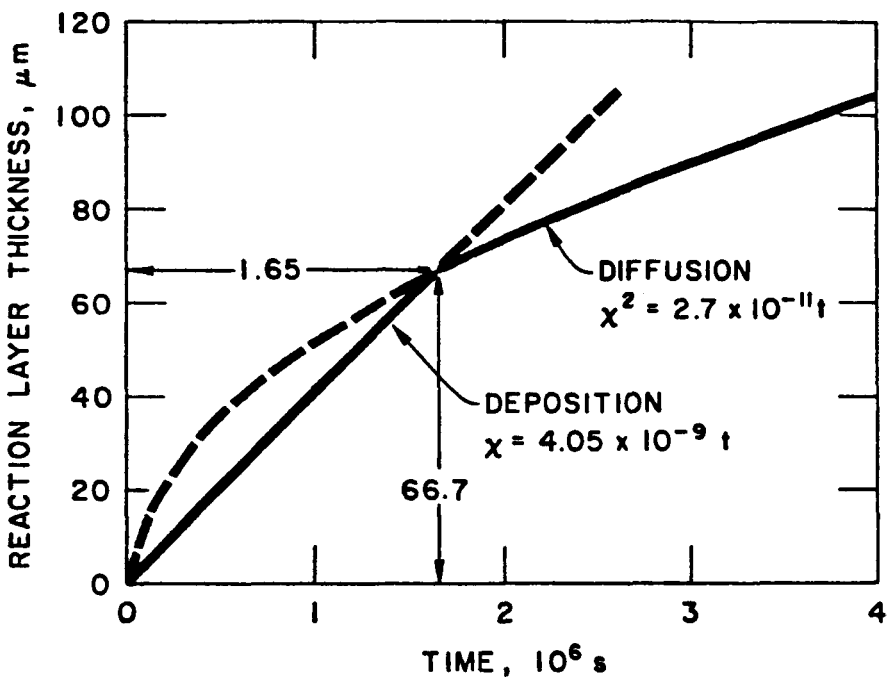

Fig. 27. Aluminum Deposition and Diffusion into Low-Carbon Steel at 475 °C

The in-cell growth of aluminum reaction layers should follow the same trend. The values for the transition time and thickness will differ, however, because the negative electrode is in the aluminum-rich discharged condition during only part of each cycle.

4. Coatings as Barriers to Diffusion

A successful barrier coating for the hardware material should undergo little or no diffusional reaction and prevent deleterious diffusion between aluminum and the substrate material. In addition, the barrier-coating material must be compatible with the electrode environment, electrically conductive, and resistant to spalling. Preliminary screening tests[14] identified chemical vapor-deposited TiC and electroplated chromium as two of the most promising coatings in terms of the latter criteria. Low-carbon steel substrates with these coatings were tested in the same manner as detailed in Section II.E.2.

A TiC coating with a thickness of 17 μm showed no microscopic evidence of reaction and maintained distinct interfaces with both the substrate and the aluminum, even after the 1000-h test period. This observation was confirmed by x-ray scanning images, such as these shown in Fig. 28 for iron, titanium, and aluminum. An SEM/EDAX* analysis of this diffusion couple showed a very low level of aluminum in both the TiC and steel regions; however, the fact that the original steel ingot was cast by the aluminum-killed process is likely to be the cause of the bulk of these counts. The TiC coating applied by the chemical vapor-deposition process appears to provide an excellent barrier to the interreaction between aluminum and substrate material.

A chromium layer with a thickness of 60 μm also appeared to prevent a reaction between the steel substrate and aluminum; however, localized areas of the chromium coating did react with the aluminum to form conical protrusions, such as the one shown in Fig. 29. After a 2000-h test, this protrusion had a base diameter of 100 μm, extended 80 μm into the aluminum and 25 μm into the chromium layer, and covered 15 to 20% of the interfacial surface area. An SEM/EDAX analysis determined that the tips of the protrusions were richer in aluminum than the balance of the protrusion. The likely compositions are Cr_2Al_{11} for the bulk of the protrusion and $CrAl_7$ for the tip. This nonplanar diffusional growth makes chromium less desirable than chemical vapor-deposited TiC for a barrier coating.

*EDAX = energy dispersive x-ray analysis.

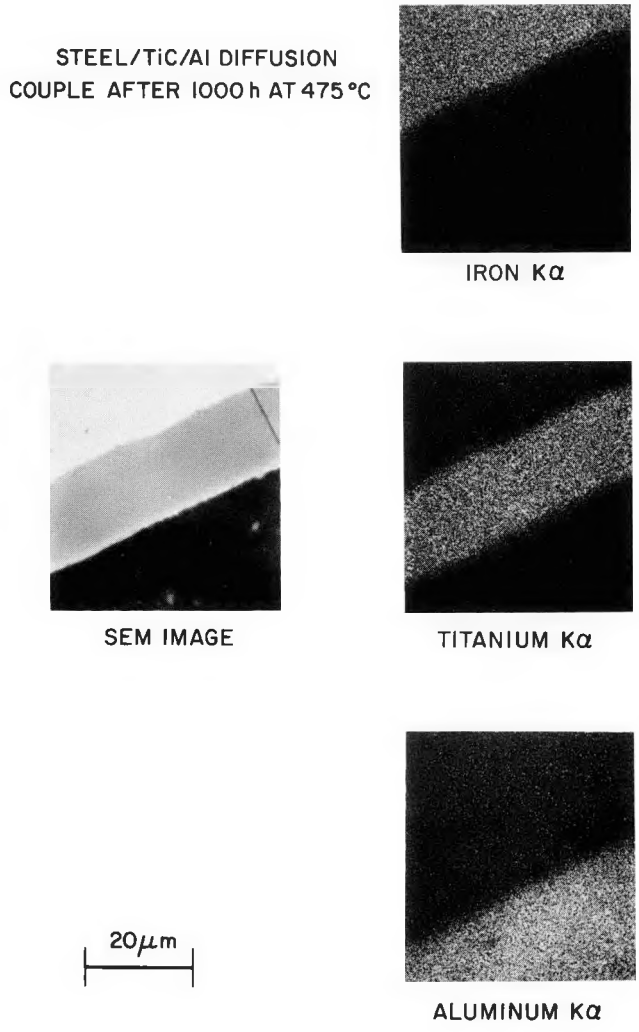

Fig. 28.

X-ray Scanning Images of TiC-Coated Low-Carbon Steel

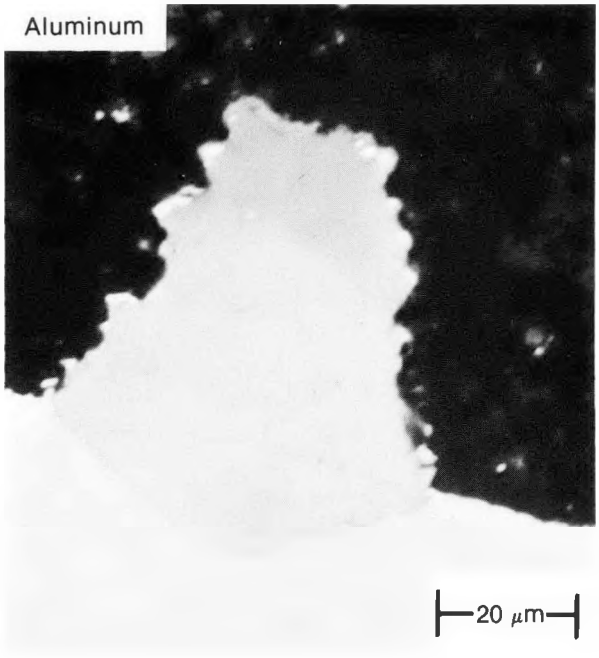

Fig. 29.

Nonplanar Diffusion for a Chromium/Aluminum Couple Tested for 1000 h at 475°C

III. LITHIUM/FeS BATTERY DEVELOPMENT PROGRAM

The lithium/FeS battery development program for FY 1982 consisted of work at ANL, Eagle-Picher Industries, Inc. (EPI), and Gould Inc. The ANL program consisted of (1) testing of Gould and Eagle-Picher cells and (2) post-test analyses of Gould and Eagle-Picher cells, as well as cell research and development. Groups of Gould and Eagle-Picher cells were subjected to lifetime testing and to tests of specific power and specific energy. The ANL cell research and development effort included cell-resistance mapping, electrode polarization measurements, computer cell design and optimization studies, thermal cycling (freeze-thaw) tests, and energy-vs.-power trade-off studies. The post-test analyses of cells included failure analysis, electrode morphology studies, and in-cell corrosion studies.

A. Testing of Gould and Eagle-Picher Cells

(W. E. Miller, J. D. Arntzen, and E. C. Gay)

The progress of the industrial contractors toward achievement of the performance goals for Li/FeS cells of (1) high reliability, (2) specific energy of 125 Wh/kg, and (3) peak specific power of 185 W/kg is monitored by periodic testing of contractor cells at ANL for cycle life and power performance. To establish cycle life for state-of-the-art cells, 12 identical cells ("status cells") supplied by the contractors are cycled to failure, which is defined as a 20% loss of capacity or a coulombic efficiency of less than 95%. To establish progress toward specific energy and power goals, both status cells and developmental cells are tested for power, energy, and cycle life as new developments become available.

1. Status Cell Lifetime Testing

Figure 30 shows the results of lifetime tests of the Eagle-Picher Group IX status cells. These Li-Al/FeS cells were built with LiCl-KCl electrolyte and BN felt separators; further design details are given in the previous annual.[15] The mean time-to-failure (MTTF) (4-h discharge rate) for the 12-cell group was 345 cycles, with a Weibull slope of 3.2. The longest life was 517 cycles and the shortest was 193 cycles. The average peak specific energy (peak specific energy for each cell is the average specific energy for cycles 6 through 10) was 90 Wh/kg for the 12 cells. Peak specific power, measured on one representative cell from the group, was 80 W/kg at 50% state of charge. For the 12-cell group, the standard deviation in discharge capacity (average 340 Ah) was ±2.1%, indicating good uniformity in cell manufacture.

The cycle life, which ranged from 193 to 517 cycles, showed a significant improvement over that of the previous group of status cells, Group VI, in which the first cell failure occurred at 100 cycles and the final one at 201 cycles. The mean time-to-failure was only 138 cycles for the Group VI cells.[16] The improvement in cycle life was a direct result of reducing the size of the openings in the photoetched electrode retainer screens (from 0.33-mm to 0.23-mm dia); this change greatly reduced the growth of protrusion from the negative electrode. Nevertheless, failures of the Group IX cells still resulted from the formation of protrusions at the Li-Al electrodes. For a discussion of cell-failure modes, see the previous annual report[17] and Section III.C of this report. None of the cells failed through capacity loss;

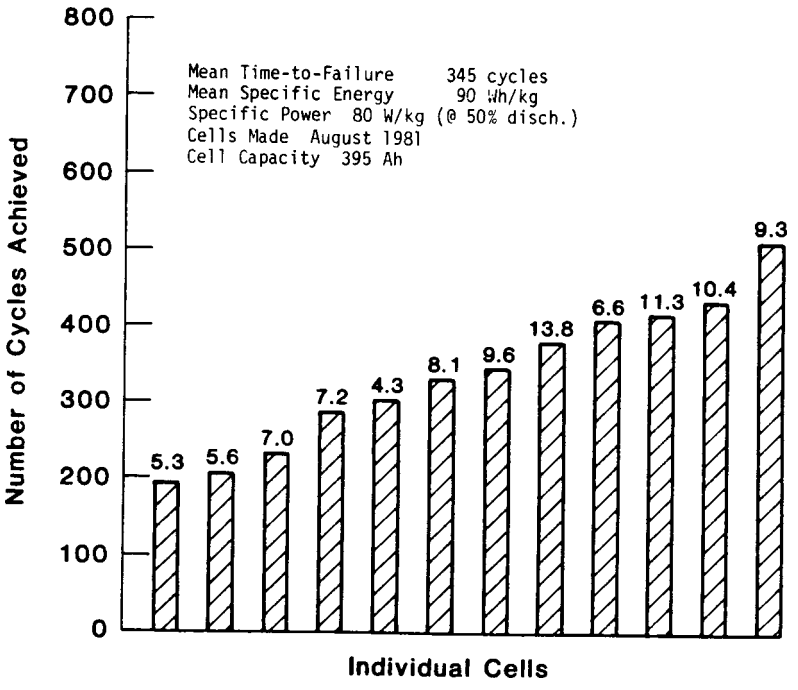

End of life defined by 20% loss of capacity or 5% loss of coulombic efficiency.
Numbers above bar show percent capacity loss.

Fig. 30. Cycle Life of Eagle-Picher Group IX Status Cells (BN felt separators)

all of them failed through short circuits. The average capacity-loss rate was 0.024% of peak capacity per cycle. This result indicates an anticipated average life, based on 20% capacity loss, of more than 800 cycles once cell short-circuit problems are solved.

Eagle-Picher has reduced the hole size in the negative electrode retainer even further by placing a 200-mesh screen (opening size, 0.074 mm) between the photoetched retainer and the electrode face. Five of these cells are on cycle at ANL. All five have achieved more than 150 cycles at this time with no loss in coulombic efficiency.

Lifetime testing was completed on a second group of status cells with MgO powder separators from Gould. These cells were built with separators of pressed MgO powder, instead of BN felt; were electrolyte-deficient; used an all-lithium electrolyte (22 mol % LiF-31% LiCl-47% LiBr); and contained a mixture of Li-Si and Li-Al for the negative electrode material. The test results for different operating temperatures are shown in Fig. 31. The mean time-to-failure at 455°C (the operating temperature recommended by Gould) was 268 cycles (Weibull slope, 3.1). The average specific energy for the 12-cell group was 80 Wh/kg at the 4-h rate. The average capacity was 157.6 Ah, with a standard deviation of $\pm$3.2%. Subsequent operation at higher temperature increased the MTTF to 330 cycles (Weibull slope 2.9). All cell failures at the initial operating temperature, 455°C, were by the 20% capacity loss

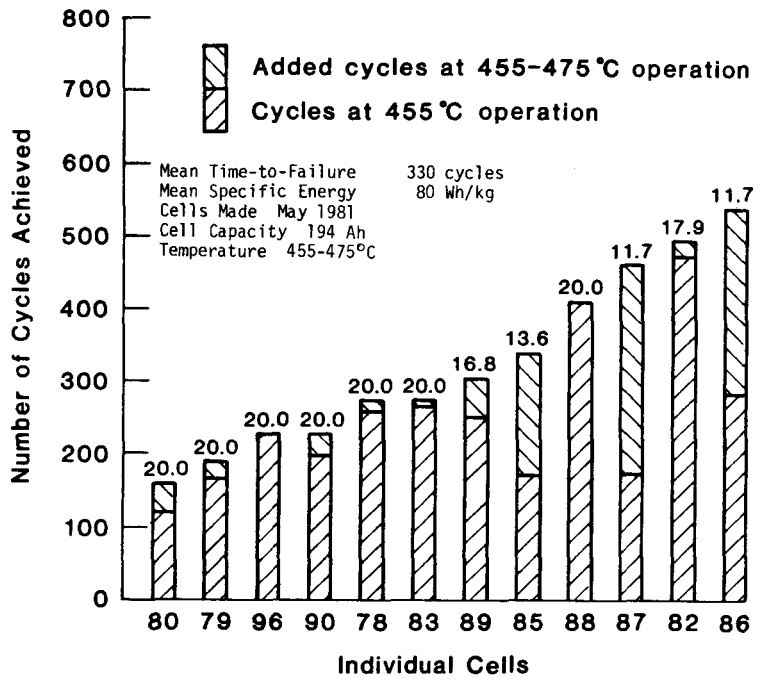

Fig. 31. Cycle Life of Gould's Second Group of Status Cells (MgO powder separators)

criterion. At increased temperature, capacity loss was less than 20% in all but one cell; and, in one other cell, a short circuit (coulombic efficiency dropped to <95%) coincided with the 20% capacity loss at 455°C. In ten cases out of eleven, raising the temperature restored the capacity to the extent that additional cycles were logged; the range was 5 to 260 additional cycles. A 5°C temperature increase from 455°C was equally effective in restoring cell capacity, as was a 10°C increase; when capacity again declined after the initial temperature change, subsequent temperature changes had little effect. The abnormal temperature sensitivity of these cells is attributed to the use of the high-melting-point (430°C) electrolyte of LiF-LiCl-LiBr. The average capacity loss rate for operation at 455°C was 0.08% per cycle. When cycles were added by raising the temperature, the average fading rate decreased to 0.06% per cycle.

2. Specific Power and Specific Energy Measurements

Cell capacity and specific energy were measured as a function of rate of discharge for representative cells from the Eagle-Picher and Gould status and development cells. Specific energy curves are shown in Fig. 32, and results of power measurements are given in Table 14.

In Fig. 32, Curves 1 and 3 are for development cells; Curves 2 and 4 are for the latest Eagle-Picher and Gould status cells, respectively. For both contractors, the major difference in the development cells and the status

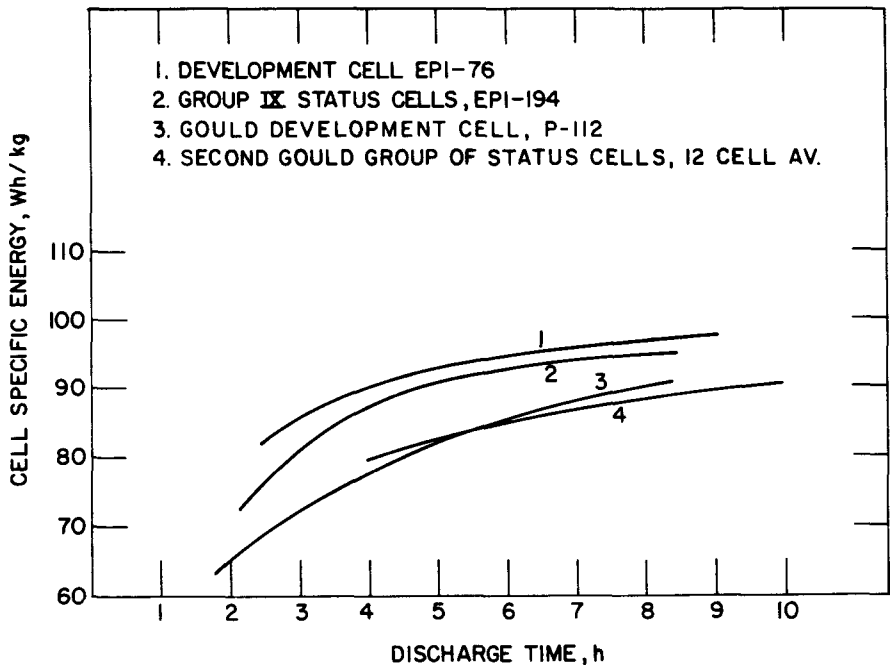

Fig. 32. Specific Energies as Function of Discharge Rate for Gould and Eagle-Picher Cells

Table 14. Peak Power at 50% SOC for Gould and Eagle-Picher Cells

Cell No.	Cell Capacity, Ah	Cell Peak Power, W	Cell Weight, kg	Specific Power, W/kg
EPI-176	394	497	4.79	104
EPI-194	394	371	4.63	80
Gould-P-112	194	351	2.69	130
Gould Status Cells[a]				70

[a]Power test was made at Gould on a representative cell.

cells was in the size of the positive terminal feedthrough and electrode connectors. In the Eagle-Picher cells, the copper core in the positive feedthrough was increased from 0.63-cm to 0.95-cm dia; in the case of the Gould cells, the diameter was increased from 0.63 cm to 1.27 cm. This change had only a modest effect on specific energy for the discharge times shown in Fig. 32. Table 14 shows the results of power measurements made on the same group of cells. The larger feedthrough increased the power by 30% in the case of the Eagle-Picher cells, and that of the Gould cells by more than 80%.

3. Progress Assessment

Table 15 summarizes the performance of all status cell groups tested at ANL to date, four groups from Eagle-Picher and two from Gould. The table shows a definite trend toward improvement in cell performance as the contractors gained experience. The second group of Gould cells had noticeably improved cycle life, less deviation from the average capacity (more uniform performance), and higher specific energy. Eagle-Picher status cells showed a gradual increase in specific energy while high cycle life was maintained. The third group of Eagle-Picher status cells (Group VI) showed a noticeable decline in cycle life, although performance was more uniform and specific energy and peak power were increased. The cells built after Group III had noticeably higher performance as a result of better utilization of active materials in the cell, i.e., 88% for Group VI, compared with 75% for Group III. It is believed that the better utilization resulted from improved electrolyte wetting of the separator, achieved by incorporation of a wetting agent in the separators. Better utilization of the active materials in the Group VI cells resulted in greater expansion forces, which promoted protrusion growth out of the negative electrode and resulting short circuits. This problem was partially solved by using electrode particle retainers with smaller holes in the Group IX cells; the mean time-to-failure increased from 138 to 345 cycles. Because negative electrode protrusions were still the major cause of failure in Group IX cells, it is expected that the present development cells under test, in which the hole size has been reduced further, will demonstrate longer cycle life.

4. Behavior of Operating Cells after Short Circuiting

One criterion for failure in the Li-Al/FeS status cell testing program has been decrease in coulombic efficiency to <95%. Lifetime testing of the status cells is terminated on the basis of this criterion. However, such a cell failure would not necessarily terminate battery operation in a series-connected battery. Operation of a series-connected, ten-cell module containing failed cells was described in a previous report.[18]

In a test of Eagle-Picher cells that were continued on cycle after a short circuit had developed, a timed cycle (3 h) was used for discharge at a 94-A constant current (282 Ah capacity). On charge, the same amount of capacity (282 Ah) is passed through the cell at a constant current of 40 A. This simulates cycling of a failed cell as part of a series string in a battery. The cell voltage and the average heat-generation rate were measured during cycling.

Table 15. Summary of Li/FeS Cell Performance Tests at ANL

	Gould Status Cells			Eagle-Picher Status Cells			
	I	II		Group I	Group III	Group VI	Group IX
No. of Cells in Group	12	12		14	12	12	12
Theo. Capacity, Ah	194	194		360	394	394	394
Av. Operating Temperature, °C	465	a		465-475	475-490	470-480	465
Av. Peak Capacity, Ah	158	157		288	294	347	340
Std. Deviation in Peak Capacity, ± %	4.5	3.2		5.2	6.6	0.9	2.1
Av. Specific Energy, Wh/kg	74	80		71	81	94	90
Peak Specific Power, W/kg	70	70		55	55	74	80
Cycle Life[b]							
High/Low, Cycles	307/14	467/121	542/158	1031/238	908/23	201/100	517/193
Mean Time-to-Failure, Cycles	218/26[c]	268	330	410	362	138	345
Weibull Slope	2.0/3.4	3.1	2.9	2.9	1.4	2.1	3.2
Av. Capacity Loss Rate, % per cycle		0.08	0.06	0.032	0.027	0.045	0.024

[a]Temperature was 455°C until 20% capacity loss, then raised in 5° increments to 455-475°C (see text).

[b]End of life defined as 20% capacity loss or coulombic efficiency decrease to <95%.

[c]Correlated as five- and seven-cell groups. Single group correlation not possible.

The behavior of cells that were cycled in the above manner is shown in Fig. 33. The numbers on the voltage curves (1 to 4) depict changing voltage conditions that result as cycling is repeated. The numbers on the heat generation curves correspond to the condition of the cell shown on the voltage curves.

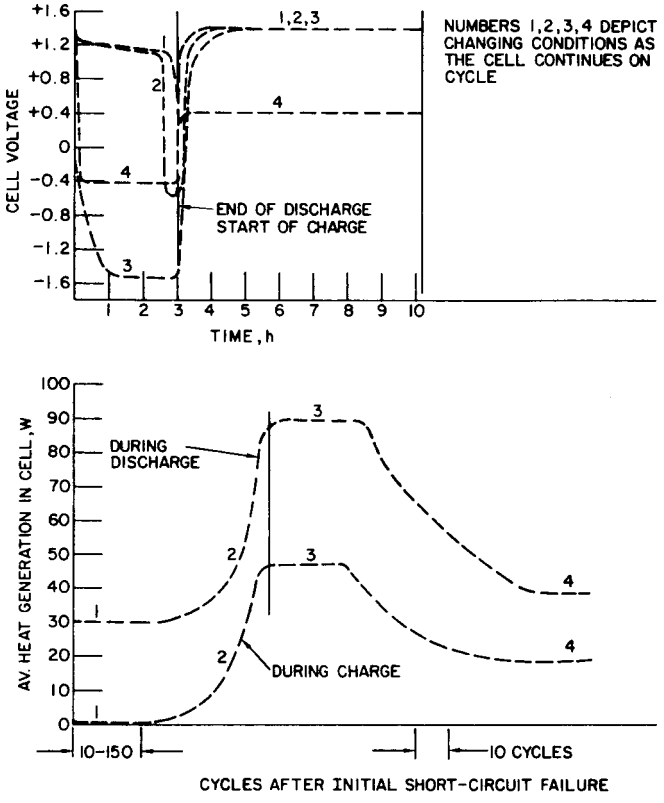

Fig. 33.

Typical Voltage and Heat-Generation Behavior in Short-Circuited Cells on Continued Cycling

State 1 results as soon as the cell is taken off voltage control. Positive voltage is maintained through most of the discharge period, with the cell voltage becoming negative only near the end of discharge, and the cell recharges to +1.4 V. Useful energy is stored in the failing cell during this period. This state lasted between 10 and 15 cycles for the four cells tested. Average heat generation in this state is 30-32 W on discharge and zero on charge.

State 2 begins with the cell voltage dropping earlier in the discharge of each cycle, until it is negative throughout the discharge, and then terminates in State 3. The heat-generation rate rises in each cycle during both discharge and charge in State 2 and peaks in State 3. The duration of State 2 is typically 30-40 cycles. State 3 is the condition where the cell is at peak negative voltage discharge and peak heat generation. Peak negative voltage is typically -1.4 to -1.6 V; peak heat generation is 90-100 W on discharge and 45-50 W on charge. The duration of these peak conditions has been 15-30 cycles. The cell then tends toward its end state, State 4. Between States 3 and 4, the voltage on discharge becomes progressively less negative

and the maximum voltage achieved during charge drops. In addition, the heat-generation rate declines with cycling. The period between the peak of State 3 and end of State 4 is, typically, approximately 50 cycles. State 4 is the end state, where conditions remain unchanging with continued cycling. Typical voltage conditions for the end state is -0.4 V on discharge and +0.4 V during charge. Heat generation is approximately 35-40 W on discharge and 15-20 W on charge.

B. ANL Cell Research and Development Program

The ANL cell research and development effort deals primarily with the overall optimization of cells and electrodes. The effort is divided into electrode-polarization measurements, resistance mapping, thermal (freeze-thaw) cycling tests, and energy-power trade-off studies.

1. Resistance Mapping
(T. D. Kaun and E. C. Gay)

Resistance-mapping measurements on state-of-the-art cells were made to determine the resistance of the various current-carrying elements of the cell, to determine improved designs of these components for lower cell resistance, and to fabricate and test higher-power cells with the lower resistance cell components.

Results of the resistance measurements for Cell EPI-111 are shown in Table 16. The total cell resistance was 1.31 mΩ. Approximately 49% of the cell resistance was external to the electrode stack and had the following distribution: 18% in the positive interelectrode connectors, 9% in the negative interelectrode connectors, 9% in the negative terminal, and 13% in the positive terminal.

Results of the resistance measurements for an improved cell design (LCMP-8) with lower-resistance components are shown in Table 17. This cell was designed and fabricated at ANL, and has approximately the same capacity as EPI-111. The objective was to reduce the cell resistance external to the electrode stack. This objective was accomplished. Of a total cell resistance of 0.47 mΩ, only 0.08 mΩ resistance (17%) was external to the electrode stack. The improvement resulted from (1) increasing the size of the cell terminals and using copper-cored negative and positive terminals, (2) using nickel interelectrode connectors and electrode tabs, instead of steel as was used in EPI-111, and (3) increasing the width of the electrode tabs from 1.0 to 6.4 cm. These improvements were later used in cells fabricated by Gould and Eagle-Picher.

2. Thermal Cycling of Li-Al/FeS Cells
(F. J. Martino and E. C. Gay)

The thermal cycling studies, which were initiated to characterize the effects of temperature changes (room temperature to 460°C) on cell performance, have been completed. A summary of the results for four full-size Li-Al/FeS cells is shown in Table 18. The cells were of identical construction, except that the BN felt separator was treated with different wetting agents.

Table 16. Resistance-Mapping Measurements on Cell EPI-111

Cell Component[a]	Resistance, mΩ
1 to 2	0.175
4 to 5	0.110
3 to 4	0.115
2 to 6	0.230
Electrode Stack (50% SOC)	0.680
Total	1.310

[a]The resistance measurement points are numbered as follows:

1. Positive Cell Terminal (6.3 mm-dia copper core)
2. Positive Interelectrode Connector (3.2 mm-thick steel)
3. Negative Electrode Housing (9.9 mm-wide tab)
4. Negative Interelectrode Connector
5. Negative Cell Terminal (6.3 mm-dia steel)
6. Positive Electrode Housing

Table 17. Resistance-Mapping Measurements on ANL Cell LCMP-8

Cell Component[a]	Resistance, mΩ
1 and 5	0.05
2 and 4	0.03
Electrode Stack (50% SOC)	0.39
Total	0.47

[a]Resistance measurement points are numbered as follows:

1. Positive Cell Terminal (9.5 mm-dia copper core)
2. Positive Interelectrode Connector (4.8 mm-thick nickel)
3. Negative Electrode Housing (6.3 cm-wide nickel tab)
4. Negative Interelectrode Connector (4.8 mm-thick nickel)
5. Negative Cell Terminal (1.3 mm-dia copper core)
6. Positive Electrode Housing (6.3 cm-wide nickel tab)

Table 18. Summary of Thermal (Freeze-Thaw) Cycling Tests of Li-Al/FeS Bicells

Cell Designation	MFT0	MFT1	MFT2	MFT3
BN felt treatment	Dusted with powdered LiCl-KCl	$LiAlCl_4$	MgO	MgO
Thermal cycles	27	38	68	16
Deep discharge cycles	227[a]	217[b]	440	101[c]
Capacity loss, %	21.6	7.4	7.0	2.7
Capacity loss/cycle, %	0.095	0.034	0.020	0.027

[a]Voluntary termination; test completed.

[b]Terminated as a result of cycler malfunction.

[c]Termination due to short circuit between electrodes (identified later by post-test examination).

Numerous thermal (freeze-thaw) cycles were conducted over successive deep-discharge cycles. With the exception of the baseline cell containing the untreated felt, the cells exhibited good performance stability, with as many as 68 thermal cycles for one cell. The overall capacity losses were no greater than those shown by similar cells that were not subjected to repeated thermal cycling.

Post-test examinations of the thermally cycled cells showed that: (1) the BN felt separators in cells in which wetting agents had been used were completely filled with electrolyte, (2) there were no differences in the physical appearance of cells that had been thermally cycled and cells that had not, (3) no cell failures were caused by failures in the BN felt separators, which retained their integrity during thermal cycling, and (4) the electrode morphology of thermally cycled cells appeared to be the same as that of cells that were not thermally cycled.

3. Cell Energy-Power Trade-Off Studies

The program goals for the Li-alloy/FeS electric-vehicle cells are to develop cells with 150- to 350-Ah capacities, specific energy of 125 Wh/kg at the 3-h discharge rate, peak power of 185 W/kg at 50% state of charge, and mean time-to-failure of 500 cycles. Development of such high-performance cells with a power-to-energy ratio of 1.5 requires that particular attention be given to energy-power trade-off studies and cell designs that do not compromise cycle life.

a. Experimental Cells
(T. D. Kaun)

The initial effort in the development of high performance cells at ANL was directed toward the demonstration of high power capability in cells of greater than 150-Ah capacity. The design of these cells included a porous facial current collector that also served as the electrode housing. Measurements were made to determine the contribution to cell power of the size and type of material used for the cell terminals and interelectrode connections.

A summary of the five cells tested in 1981-82 is shown in Table 19. The range of specific energy for these cells was 77 to 101 Wh/kg. At 50% state of charge, peak power ranged from 129 to 192 W/kg. The power-to-energy ratios were from 1.3 to 2.5. The major improvement in power for these cells, compared with earlier ones, was due to reduction in resistance in the terminals, interelectrode connectors, and electrode tabs.

Table 19. Performance of Li-Al/FeS Cells Designed to Improve Power (tested in 1981-1982)

Specific Energy,[a] Wh/kg	Specific Power, W/kg		Number of Cycles Tested
	95% SOC	50% SOC	
77	233	192	94
88	142	129	100
92	178	130	>180
101	180	132	75
98	208	161	106

[a]Measured at 3.4-h discharge rate.

Efforts at ANL to fabricate a cell with specific energy greater than 100 Wh/kg at the 3-h discharge rate, without sacrifice of high power, were also successful. The performance of this cell, LCMP-17, and recent Gould and Eagle-Picher cells are compared in Table 20. The improvement in the performance of Cell LCMP-17 is attributed to the following design features: (1) additives to the Li-Al electrode allowed a reduction in the negative-to-positive capacity ratio (0.8 compared with 1.3 and 1.6 for Eagle-Picher and Gould cells, respectively), which resulted in good utilization and stable capacity with cycling, and (2) the combined current collector-housing weight for Cell LCMP-17 was reduced by making the housing part of the current collector for the positive electrode. In the Gould and Eagle-Picher cells, the negative electrodes are in direct contact with the housing. A weight analysis of the three cells is shown in Table 21.

Table 20. Performance of Li-Alloy/FeS Development Cells Fabricated by ANL and Contractors

Cell Characteristic	EPI-176	Gould Cell 112	LCMP-17
Specific Energy,[a] Wh/kg	87	72	101
Specific Power,[b] W/kg	104	130.5	132
Utilization,[a] %	85.3	80.0	76
Power-to-Energy Ratio	1.2	1.8	1.3
Cycle Life	109	110	75
Theoretical Capacity, Ah	394.8	194	370
Total Cell Weight, kg	4.793	2.693	3.325

[a]Measured at the 3.4-h discharge rate.

[b]Measured at 50% state of charge.

Table 21. Weight Analysis of Improved Performance Li-Alloy/FeS Development Cells

Cell Component	Percentage of Total Cell Weight		
	EPI-176	Gould Cell-112	LCMP-17
FeS	13.5	12.3	21.7
Li-Al	15.5		14.1
Li-Al-Si		12.1	
Electrolyte	28.0	23.9	25.6
Current Collector	23.5	22.0	23.5
Cell Housing	12.3	15.4	8.9
Feedthrough Assemblies	4.3	9.8	4.1
BN Felt	2.9		2.1
MgO Powder		4.5	

b. Computer Cell Design and Optimization Studies
(E. C. Gay)

A computer program for the design and optimization of Li-alloy/iron sulfide cells was described in Section II.D.2 of this report.

Cell LCMP-17, described in the preceding section of this report, has achieved the highest combination of specific energy and specific power for a Li-alloy/FeS cell tested to date. With the cell design program, calculations were made to determine the effect of cell capacity and power-to-energy ratio on the performance of cells with the same general design characteristics (such as electrode size, thickness, and loading density) and electrode utilization as Cell LCMP-17.

The design characteristics and achieved performance for Cell LCMP-17 are shown in Table 22; the design characteristics and projected performance calculated with the computer model are also given in this table. A comparison of the calculated and measured performance showed good agreement. The specific energy and specific power as a function of cell capacity and power-to-energy ratio are shown in Fig. 34. These results show that if a cell with the design given in Table 22 were capable of delivering 125 Wh/kg (a power-to-energy ratio of 0.6) at the 3-h discharge rate at a capacity less than 400 Ah, then the maximum peak specific power would be 75 W/kg at 50% state of charge. At a peak specific power of approximately 145 W/kg at 50% state of charge, the specific energy would decrease to ∿95 Wh/kg (a power-to-energy ratio of ∿1.5) at a cell capacity of 400 Ah.

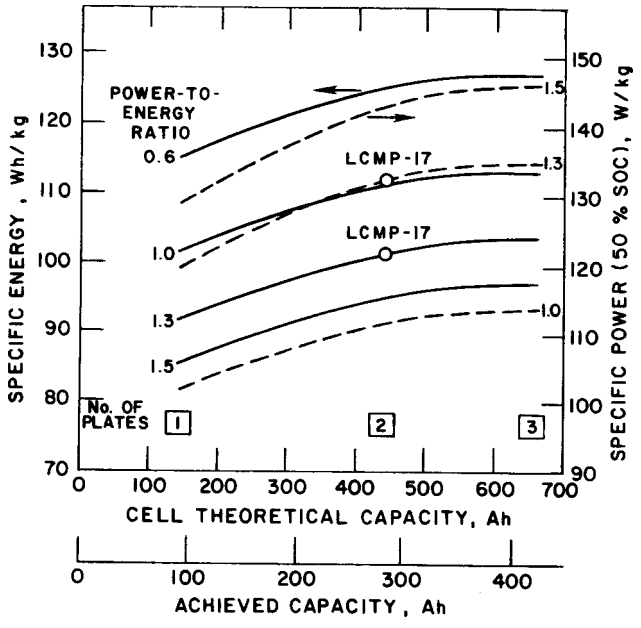

Fig. 34.

Specific Energy and Power as a Function of Cell Capacity Calculated for Li-Al/FeS Cells

Table 22. Design and Performance Correlation for Li-Al/FeS Cell

	Cell LCMP-17	Calculation from Computer Model
Positive Electrode		
Size, cm x cm	12.5 x 17.5	13.2 x 17.5
Carbon Additive Weight, g	85.0	85.0
Theor. Capacity, Ah	440.0	440.6
Thickness, cm	0.7	0.70
FeS Weight, g	721.0	722.0
Active Material Loading Density, Ah/cm^3	1.4	1.4
No. of Parallel Electrodes	3[a]	2[a]
Electrode Utilization, %	64.0	64.0
Negative Electrodes		
Theor. Capacity, Ah	370.0	370.0
Thickness, cm	1.0	1.0
50 at. % Li-Al Weight, g	468.3	468.5
Active Material Loading Density, Ah/cm^3	0.85	0.87
No. of Parallel Electrodes	2[a]	3[a]
Negative-to-Positive Capacity Ratio	0.84	0.84
Carbon Additive Weight, g	81.7	82.0
Electrode Utilization, %	76.2	76.2
Electrolyte Weight (54 wt % LiCl-KCl), g	850.0	832.2
Current Collector		
Pos. Perforated Particle Retainer Thickness, cm	0.025	0.033[b]
Neg. Perforated Particle Retainer Thickness, cm	0.046	0.033[b]
Total Current Collector Weight, g	>755[c]	857.9
Open Area Fraction of Perforated Plate	0.55	0.55
Terminal Diameter, cm	0.95 (neg)[d]	0.94 (neg/pos)
Cell resistance, mΩ	0.9	0.97
Cell Housing		
Thickness, cm	0.038	0.038
Weight, g	295	255.6
Total Cell Weight, kg	3.325	3.325
Specific Energy (C/3), Wh/kg	103	102
Specific Power (50% DOD), W/kg	136	132
Power-to-Energy Ratio	1.3	1.3

[a]Total number of plates is the same in the two designs.

[b]Based on the difference between the design of LCMP-17 and the model (positive electrode grounded vs. center electrodes), these are equivalent dimensions.

[c]Positive electrodes were grounded to cell housing; fraction of housing weight contributing to current collection for positive is not included in the current collector weight shown.

[d]Positive grounded to cell can; center sheet of cell can was 70 g, 0.25 mm-thick copper sheet covered with steel sheet.

It was concluded that the basic state-of-the-art cell designs are insufficient to meet both the specific energy and the specific power goals. Improvements in the electrode compositions are needed that will provide either higher specific capacity (Ah/g) and/or higher average discharge voltage and, hence, better power characteristics are needed. Improved current-collector designs for higher utilization in thick positive electrodes are also needed. Possible improvements are the use of Li-Al-Fe and Li-Si negative electrodes. The present cell terminals and interelectrode connectors are believed to be adequate to meet the performance goals.

C. Post-Test Analysis of Gould and Eagle-Picher Cells
(J. E. Battles, F. C. Mrazek, and A. A. Ziegler)

Post-test examinations, which have been an important part of the Li-Al/FeS battery development program, have provided valuable information for recommendations on designs to achieve improved cell performance and reliability and for the selection of materials. The major objective of the post-test examination has been the determination of cell-failure mechanisms. Other objectives are (1) the determination of the electrode microstructure, (2) the distribution, uniformity and utilization of active materials, and (3) the in-cell corrosion of current-collector materials. Post-test examination methods include metallography, chemical analysis, X-ray diffraction, ion and electron microprobe analysis, and scanning electron microscopy. Because the cell materials (LiCl-KCl, LiAl, Li_2S) react rapidly with the ambient atmosphere, a unique helium-atmosphere facility was constructed for the post-test examination of cells. The results to be presented in this section of the report pertain to failure analyses of Eagle-Picher and Gould status cells, the microstructure of the Li-Al electrode, and the in-cell corrosion of current-collector materials.

1. Eagle-Picher Cells

Failure analyses have been completed for the Eagle-Picher Groups I, III, VI, and IX status cells; the failure modes are summarized in Table 23. In all cases, failure resulted from an electrical short circuit between opposing electrodes, which was indicated by a decline in the coulombic efficiency. Two major failure modes have been identified. The first is the formation of Li-Al protrusions that penetrate the BN felt separator and contact the positive electrode. A typical example of a protrusion, with the porous structure typical of the negative electrode, is shown in Fig. 35. This failure mode was most prevalent in the Groups III, VI, and IX cells, and it coincided with a change in methods of cell assembly and pretreatment of BN felt separators; i.e., present BN felts are saturated with magnesium acetate or nitrate, compressed, then pyrolyzed before assembly, whereas previous felts were untreated and compressed during cell assembly. Although the mechanism for the formation of Li-Al protrusions has not been completely elucidated, recent studies have shown that they can be prevented by simple mechanical design changes. The mean time-to-failure (MTTF) for the Group IX cells was significantly extended over that of the Group VI cells; this improvement was accomplished by reducing the size of the openings in the photoetched retainer screens (from 0.33-mm dia to 0.23-mm dia). Post-test examination of the Group IX cells showed that, although the failures were caused by protrusions, the number of protrusions was considerably less than that observed in the Group VI cells. Additional cell tests have shown that protrusion formation can be completely prevented by incorporating fine mesh screen inside the normal photoetched retainer screen.

Table 23. Failure Analysis of Eagle-Picher Status Cell Groups I, III, VI, and IX

Failure Mechanisms	Number
Li-Al Protrusions across BN Felt Separator	26
Extrusion of Active Material from Ruptures in the Electrode Edge Retainers	9
Short Circuit in Feedthrough	1
Assembly Difficulty	3
Other	3
Not Identified	3
Not Examined	5
TOTAL	50

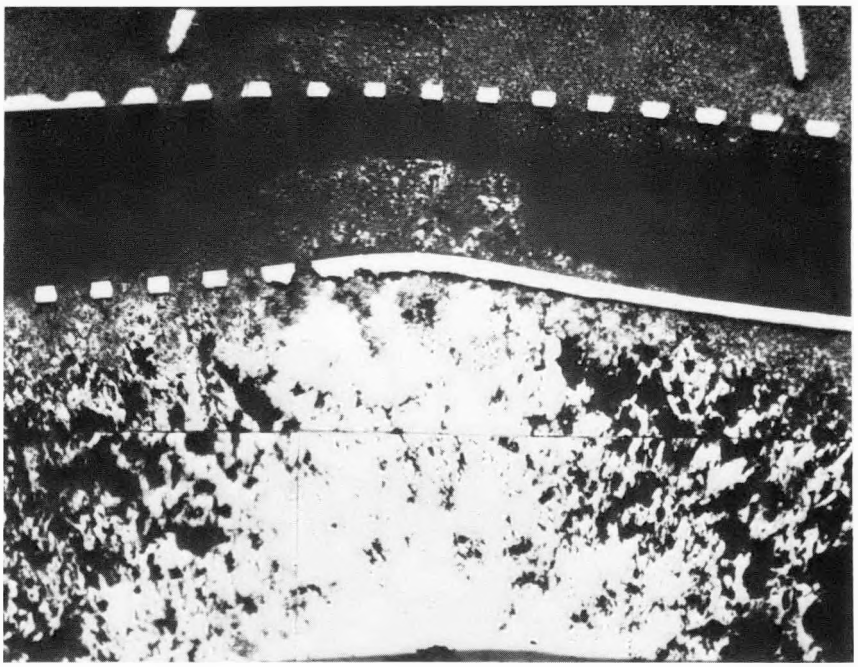

Fig. 35. Penetration of BN Felt Separator by Li-Al Protrusion (the major cause of short-circuit failure in Eagle-Picher Groups III, VI, and IX Status Cells).

The second major cause of short-circuit failures in Eagle-Picher status cells was the extrusion of active materials at the edge of the electrodes. An example of this failure mode is shown in Fig. 36, where the positive electrode material has extruded through a rupture in the edge retainer and contacted the negative electrode. This failure mode, which was caused by inadequate mechanical restraint at the electrode edges, was the predominant cause of short-circuit failures in the Group I cells. No additional extrusion failures have occurred since a U-shaped channel was added to reinforce the mechanical restraints at the edges of both electrodes.

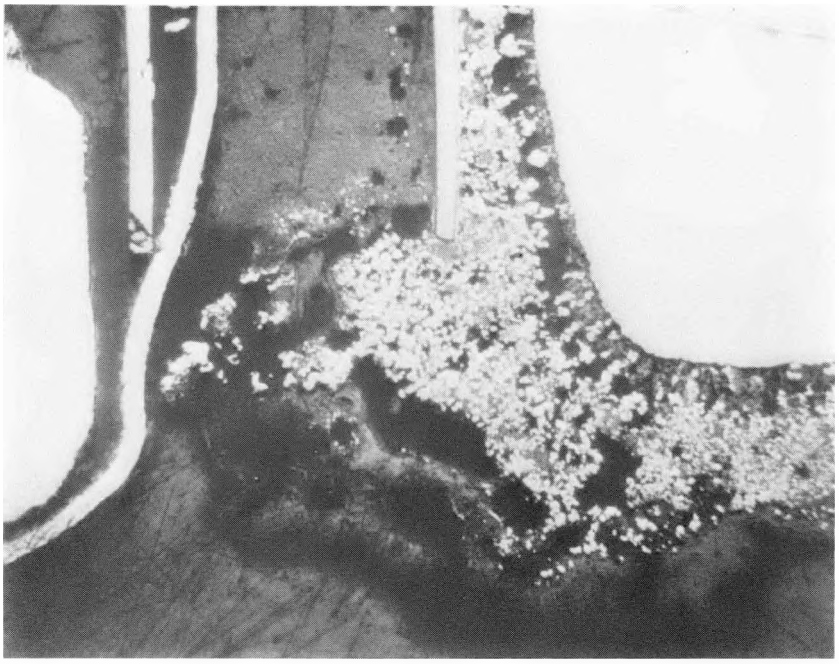

Fig. 36. Example of a Cell Failure Caused by Extrusion of Positive Material Through a Rupture in the Electrode Retainer (Cell EP-051).

2. Gould Cells

Post-test examination of the two groups of Gould status cells showed only a single mechanism for the internal short-circuit failures. The failure modes are summarized in Table 24. Two cell failures were caused by short circuits in the external electrical feedthroughs. Although all of the cells in the first group and most of the cells in the second group failed because of capacity loss, cell operation was continued to the point of short-circuit failure (coulombic efficiency decline), except for two cells in the first group. In these cells, the predominant failure mode was short circuits caused by complete penetration of the MgO powder separator by active material from the positive electrode, as shown in Fig. 37. The material from the positive electrode compressed the MgO powder and its irregular advance resulted in numerous localized penetrations, which eventually contacted the negative electrode (300-500 cycles). This failure mode occurs because the mechanical

Table 24. Failure Analysis of Gould Status Cells Groups 1 and 2

Failure Mechanisms	Number
Separator Penetrated by Positive Electrode Material	9
Short Circuit in Feedthrough	2
Capacity Decline	2
Not Examined	11
TOTAL	24

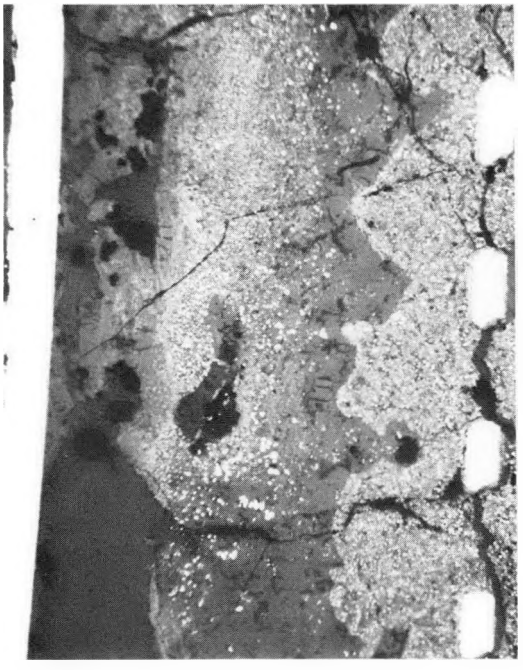

Fig. 37.

Penetration of MgO Powder Separator by Active Material from the Positive Electrode (major cause of short-circuit failures in Gould status cells).

properties of the present MgO powder separators are inadequate for containment of the positive electrode material. Elimination of this failure mechanism requires substantial improvements in the mechanical properties of the powder separator/retainer system.

Metallographic examinations of numerous negative electrodes have shown that the Li-Al alloy forms a connected, porous microstructure regardless of the state of the starting material, i.e., aluminum wire, cast Li-Al plates, and Li-Al powders. This porous microstructure is formed early in the life of the cell (<25 cycles), and it remains relatively stable throughout the life of the cell. This microstructure appears ideal for high utilization of the active material at high reaction rates, because of the open structure, high surface area, and small size of the metallic structure.

The in-cell corrosion of current-collector materials has been characterized by the use of metallography, x-ray diffraction, and electron-microprobe analysis. In FeS electrodes, intergranular corrosion of the low-carbon steel current collectors is initially very rapid, but diminishes to a low value after 200-300 days. Studies have shown that the rapid intergranular corrosion can be eliminated by the addition of excess iron powder to the FeS electrode. In the negative electrode, examinations have shown that aluminum reacts with iron and nickel current collectors to form brittle, intermetallic compounds. This reaction occurs by the galvanic deposition of aluminum at the end of discharge when the Li-Al alloy is depleted of lithium. This relatively slow reaction (~20 μm/y) becomes diffusion-limited after the initial stage, in which it is limited by the transport of aluminum to the surface of the current-collector material. Studies have shown that this reaction can be reduced by maintaining excess LiAl in the electrode. Also, protective coatings are being investigated as a means of preventing this corrosion reaction.

D. Eagle-Picher Industries, Inc. and Gould Inc. Programs
(W. E. Miller and R. F. Malecha)

A summary of the battery development programs at Eagle-Picher and Gould is given below. A detailed description of the ANL test results for full-size electric-vehicle cells fabricated by these contractors is presented in Section III.A.

The FY 1982 effort at Eagle-Picher Industries, Inc. was devoted to continued development of 395-Ah capacity cells with BN felt separators. Eighteen cells were delivered to ANL during the year.

One of the major problems addressed during the past year was the improvement of cell life. The Group VI cells built and tested in FY 1981 revealed a life-limiting failure mechanism of negative electrode protrusion growth. This problem was not prevalent in earlier cells, because they had lower electrode utilizations. The development of a separator-treatment process was completed during the year, resulting in better wetting, and hence, improvement in electrode utilization. Coincident with the improved utilization came the increased protrusion growth.

The corrective action taken to prevent the negative electrode protrusions was to use electrode particle barriers with smaller hole size. The lifetime improvement was demonstrated in the Group IX cells, which had a mean time-to-failure of 345 cycles, compared with 138 in the Group VI cells. Cells built late in FY 1982 are expected to show further improvement in lifetime, with good performance, because the particle-barrier hole size was further reduced in these test cells. Five cells now on test have passed 200 cycles with no sign of short circuits.

Progress has also been made in lowering the cell resistance to increase power. The effect on cell power of a feedthrough of larger diameter was to increase the peak specific power from 80 W/kg in status cells to 104 W/kg in a development cell (EPI-176). Tooling for production of the larger feedthrough was completed late in the year for use on other development cells. These development cells are of a new design, which incorporates a centerline current collector to reduce cell resistance further.

At Gould Inc., development work on 194-Ah cells with MgO powder separators was carried out in FY 1982. Of the cells built, ten were sent to ANL for testing. Fabrication procedures were improved during the year, which helped to eliminate cell problems that had led to early failures. Cell lifetime was improved, as demonstrated by a mean time-to-failure of 330 cycles for the second group of status cells tested at ANL. A larger feedthrough was developed. A Gould cell with the larger feedthrough gave a peak specific power of 130 W/kg. Gould status cells with the old style, small feedthrough gave a peak specific power of 70 W/kg. Variables investigated in the development of cells with immobilized electrolyte and MgO powder separators included composition of the negative electrode, negative-to-positive capacity ratio, and reduction in the amount of electrolyte used. Negative electrodes with mixtures of Li-Si and Li-Al gave higher cell performance than cells with Li-Al electrodes. The Li-Si content, which does not exceed a third of the cell lithium capacity, has not had adverse effect on cell cycle life.

REFERENCES

1. D. L. Barney et al., Lithium/Iron Sulfide Batteries for Electric-Vehicle Propulsion and Other Applications, Progress Report for October 1979-September 1980, Argonne National Laboratory Report ANL-80-128, p. 67 (Feb. 1981).

2. D. L. Barney et al., Lithium/Iron Sulfide Batteries for Electric-Vehicle Propulsion and Other Applications, Progress Report for October 1979-September 1980, Argonne National Laboratory Report ANL-80-128, p. 69 (Feb. 1981).

3. D. L. Barney et al., Lithium/Iron Sulfide Batteries for Electric-Vehicle Propulsion and Other Applications, Progress Report for October 1980-September 1981, Argonne National Laboratory Report ANL-81-65, p. 14 (Feb. 1982).

4. L. Redey and D. R. Vissers, Extended Abstracts 160th Electrochem. Soc. Meeting, Denver, CO, October 11-16, 1981, Vol. 81-2, p. 589 (1981).

5. D. Warin, Z. Tomczuk, and D. R. Vissers, Electrochemical Behavior of Li_2S in LiCl-KCl, J. Electrochem. Soc., 130, 64 (1983).

6. Z. Tomczuk, S. K. Preto, and M. F. Roche, J. Electrochem. Soc., 128, 760 (1981).

7. D. L. Barney et al., Lithium/Iron Sulfide Batteries for Electric-Vehicle Propulsion and Other Applications, Progress Report for October 1980-September 1981, Argonne National Laboratory Report ANL-81-65, p. 16 (Feb. 1982).

8. Z. Tomczuk, M. F. Roche, and D. R. Vissers, J. Electrochem. Soc., 128 2255 (1981).

9. C. J. Wen, B. A. Boukamp, R. A. Huggins, and W. Weppner, J. Electrochem. Soc., 126, 2258 (1979).

10. Sulfide Mineralogy, P. H. Ribbe, Ed., Souther Printing Co., VA (1974).

11. W. Tiedemann and J. Newman, J. Electrochem. Soc., 122, 1482 (1975).

12. Private communication, P. A. Nelson, Argonne National Laboratory (1982).

13. P. A. Nelson et al., High Performacne Batteries for Off-Peak Energy Storage and Electric-Vehicle Propulsion, Progress Report for the Period July-December 1975, Argonne National Laboratory Report ANL-76-9, p. 45 (April 1976).

14. D. L. Barney et al., Lithium/Iron Sulfide Batteries for Electric-Vehicle Propulsion and Other Applications, Progress Report for October 1979-September 1980, Argonne National Laboratory Report ANL-80-128, pp. 147-149 (Feb. 1981).

15. D. L. Barney et al., Lithium/Iron Sulfide Batteries for Electric-Vehicle Propulsion and Other Applications, Progress Report for October 1980-September 1981, Argonne National Laboratory Report ANL-81-65, p. 67 (Feb. 1982).

16. Ibid., p. 39.

17. Ibid., pp. 47-54.

18. Ibid., pp. 42-46.